# Chapter 8

QCD in e^+e^- annihilations

Literature:

- Dissertori/Knowles/Schmelling [27]

- Ellis/Stirling/Webber [28]

- Bethke [29, 30]

- Particle Data Group [26]

- JADE, Durham, and Cambridge jet algorithms [31, 32, 33, 34]

- FastJet Package, Fast k_T, SISCone [35, 36, 37]

In Chap. 7, QCD is introduced as an $SU(3)$ gauge theory. Here we continue this discussion and consider QCD processes following e^+e^- annihilations. The main focus is on the definition and application of observables linking theoretical predictions with measurable quantities: Jets and event shapes are discussed; the applications include measurements of the parton spins, the strong coupling constant, and the QCD color factors. The chapter is concluded by an outlook to hadronization and non-perturbative QCD.

Some examples of e^+e^- colliders and their energies are given in Tab. 6.1. Fig. 8.1(a) maps the corresponding eras onto the available center of mass energies. A half-logarithmic plot comparing $\sigma^{e^+e^- \to \text{hadrons}}$ to $\sigma^{e^+e^- \to \mu^-\mu^+}$ is given in Fig. 8.1(b). Experimental milestones include:

- *SPEAR (SLAC):* Discovery of quark jets.

- *PETRA (DESY) & PEP (SLAC):* First high energy ($> 10\,\text{GeV}$) jets; discovery of gluon jets (at the PETRA collider, see Fig. 8.2); many pioneering QCD studies.
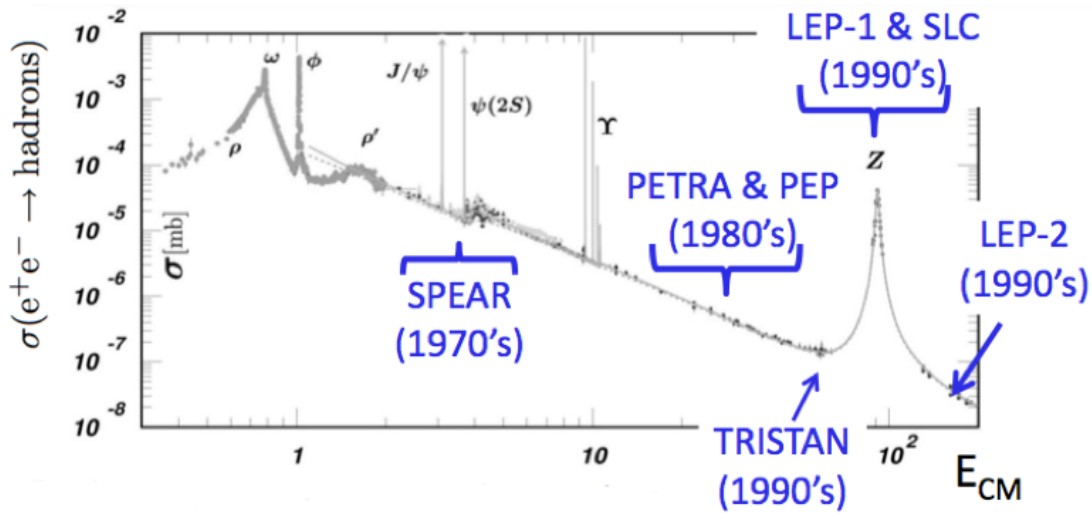
(a)
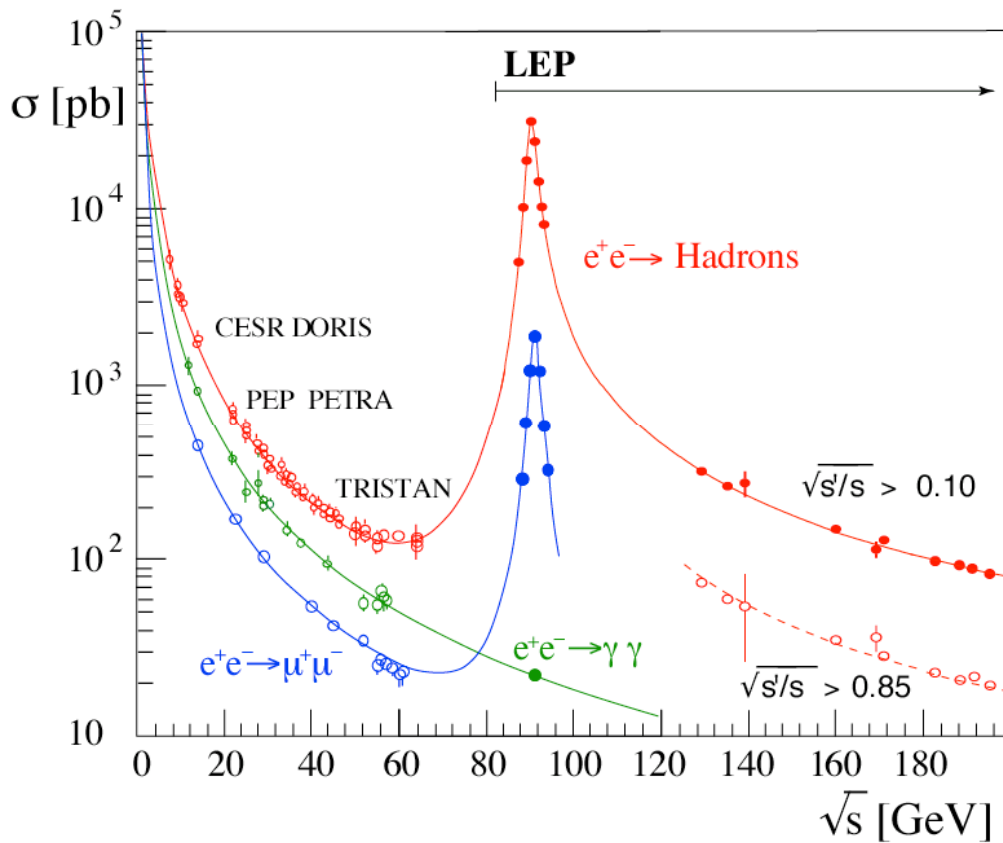
(b)

Figure 8.1: *Cross sections in e^+e^- annihilations.* (a) Cross section for $e^+e^- \to$ hadrons as a function of the center of mass energy. The E_{CM} dependence is linear because the plot is double-logarithmic. Source: [38]. (b) Comparison of cross sections for $e^+e^- \to$ hadrons and for $e^+e^- \to \mu^-\mu^+$. Both cross sections show the same $1/s$ dependence on the center of mass energy squared, except at the Z resonance.
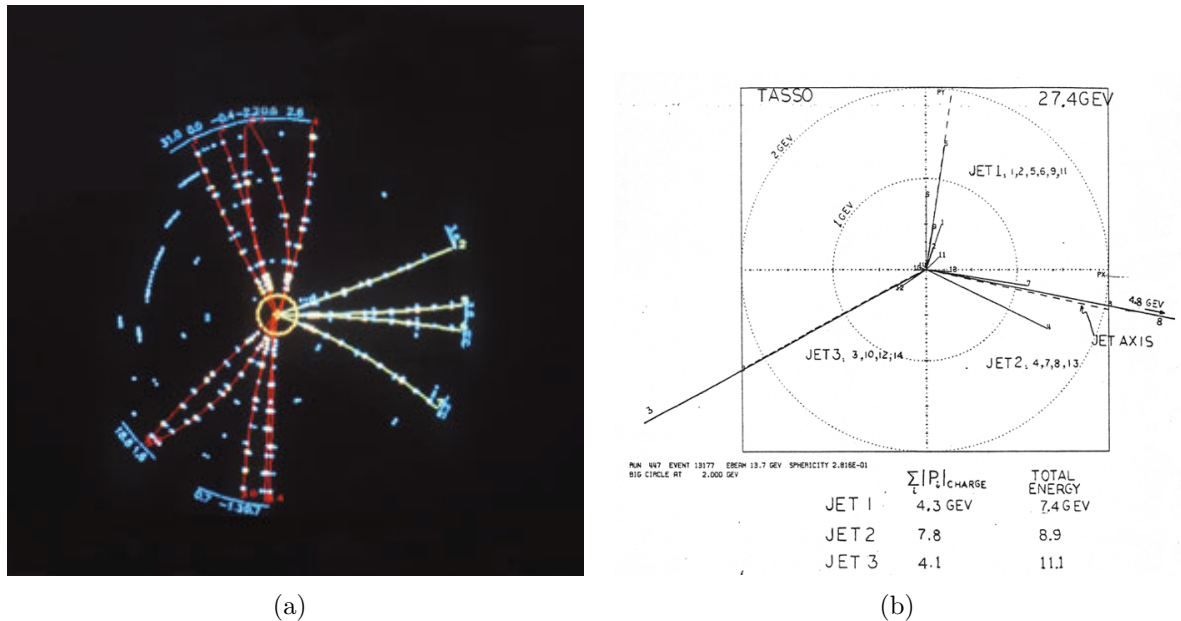
(a) (b)

Figure 8.2: *Gluon discovery at the PETRA collider at DESY, Hamburg.* Event display (a) and reconstruction (b).

- *LEP (CERN) & SLC (SLAC):* Large energies (small α_s, see later) mean more reliable calculations and smaller hadronization uncertainties. Large data samples are collected: $\sim 3 \cdot 10^6$ hadronic Z decays per experiment. This allows for precision tests of QCD.

8.1 The basic process: $e^+e^- \rightarrow q\bar{q}$

In Sect. 5.10 we calculated the cross section for $e^+e^- \rightarrow \mu^+\mu^-$ and found

$$\sigma^{e^+e^- \rightarrow \mu^+\mu^-} = \frac{4\pi\alpha_{\text{em}}^2}{3s} = \frac{86.9\,\text{nbGeV}^2}{s} \tag{8.1}$$

where the finite electron and muon masses have been neglected. Here, we consider the basic process $e^+e^- \rightarrow q\bar{q}$. In principle, the same Feynman diagram contributes:
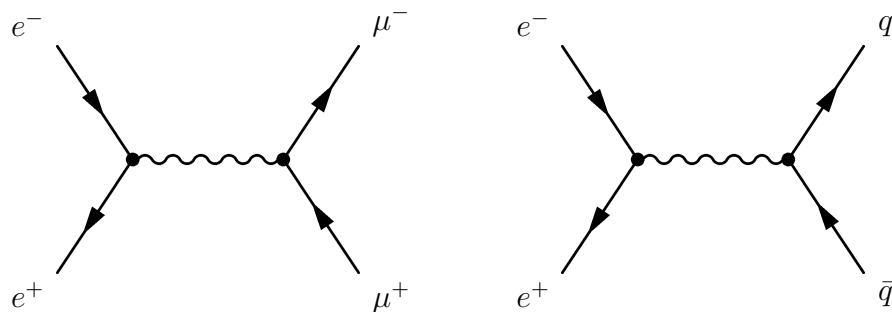
The only differences are the fractional electric charges of the quarks and the fact that the quarks appear in $N_c = 3$ different colors which cannot be distinguished by measurement. Therefore, the cross section is increased by a factor N_c. For the quark-antiquark case one thus finds (for $m_q = 0$)

$$\sigma_0^{e^+e^- \to q\bar{q}} = \frac{4\pi\alpha_{\text{em}}^2}{3s} e_q^2 N_c = \frac{86.9\,\text{nbGeV}^2}{s} e_q^2 N_c. \tag{8.2}$$

We assume $\sum_q \sigma^{e^+e^- \to q\bar{q}} = \sigma^{e^+e^- \to \text{hadrons}}$, i.e. the produced quark-antiquark pair will always hadronize.

With Eq. (8.1) and (8.2), neglecting mass effects and gluon as well as photon radiation, we find the following ratio:

$$R = \frac{\sigma^{e^+e^- \to \text{hadrons}}}{\sigma^{e^+e^- \to \mu^+\mu^-}} = N_c \sum_q e_q^2. \tag{8.3}$$

The sum runs over all flavors that can be produced at the available energy. For E_{CM} below the Z peak and above the Υ resonance (see Fig. 8.3), we expect[1]

$$R = N_c \sum_q e_q^2 = N_c \left[\underbrace{\left(\frac{2}{3}\right)^2}_{u} + \underbrace{\left(-\frac{1}{3}\right)^2}_{d} + \underbrace{\left(-\frac{1}{3}\right)^2}_{s} + \underbrace{\left(\frac{2}{3}\right)^2}_{c} + \underbrace{\left(-\frac{1}{3}\right)^2}_{b} \right] = N_c \frac{11}{9}.$$

This is in good agreement with the data for $N_c = 3$ which confirms that there are three colors. At the Z peak one also has to include coupling to the Z boson which can be created from the e^+e^- pair instead of a photon. The small remaining difference visible in the plot is because of QCD corrections for gluon radiation (see later).

8.1.1   Singularities

In order to achieve a better prediction, we have to go beyond the basic QED prediction by including QCD dynamics: Consider the production of a quark-antiquark pair along with a gluon:
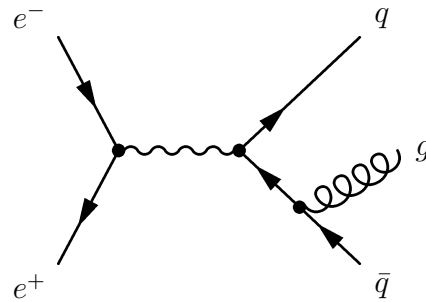
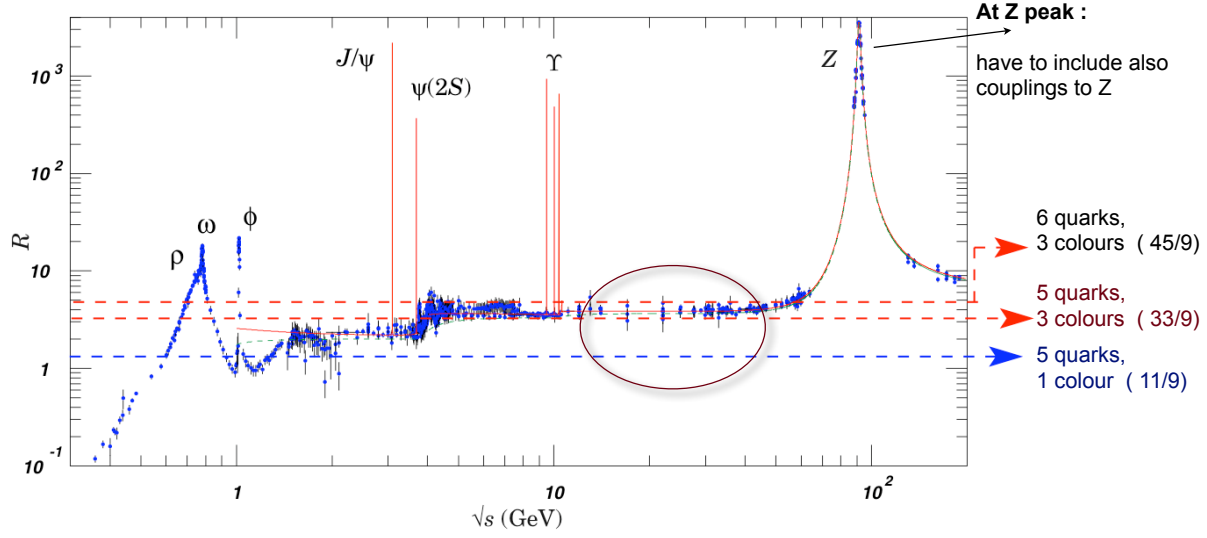[1]Recall that the top quark mass is $m_t \approx 171\,\text{GeV}$.

Figure 8.3: *Ratio* $R = \sigma^{e^+e^- \to hadrons}/\sigma^{e^+e^- \to \mu^+\mu^-}$ *as a function of the center of mass energy.* As expected by Eq. (8.3), there is roughly no energy dependence besides various resonances. The data confirm that there are three quark colors.

We define the kinematic variables

$$x_i = 2\frac{p_i \cdot Q}{Q^2} = \frac{E_i^*}{E_{\text{beam}}} \tag{8.4}$$

where $Q = p_{e^+} + p_{e^-} = p_{\gamma/Z}$ and $Q^2 = s$. Energy-momentum conservation $(\sum_i p_i = Q)$ requires that, in this case,

$$x_q + x_{\bar{q}} + x_g = 2 \tag{8.5}$$
$$x_i \leq 1. \tag{8.6}$$

One can calculate the differential cross section

$$\frac{d^2\sigma}{dx_q dx_{\bar{q}}} = \sigma_0 \frac{\alpha_s}{2\pi} C_F \frac{x_q^2 + x_{\bar{q}}^2}{(1 - x_{\bar{q}})(1 - x_q)} \tag{8.7}$$

where $C_F = 4/3$ is the color factor of the fundamental representation. Note that this expression is singular for

- $x_q \to 1$, e. g. $\bar{q}\|g$,

- $x_{\bar{q}} \to 1$, e. g. $q\|g$, and for

- $(x_q, x_{\bar{q}}) \to (1, 1)$, e. g. $x_g \to 0$.

Because of the kinematic constrains imposed by energy-momentum conservation (Eq. (8.5) and (8.6)), the allowed region (part of which we have to integrate Eq. (8.7) over to find a cross section) for a $\gamma^\star \to q\bar{q}g$ event is of the form shown in Fig. 8.4.
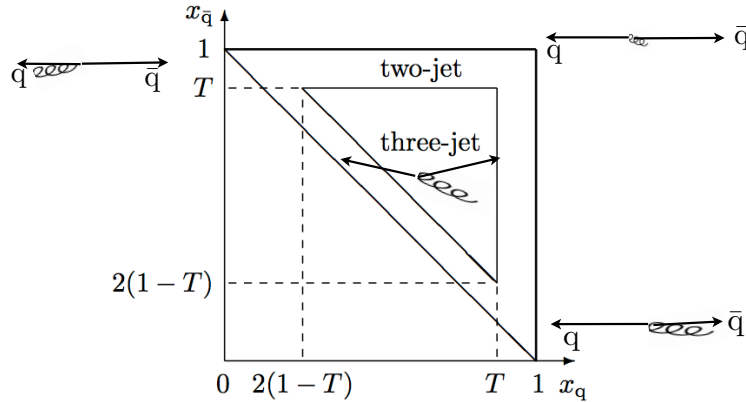
Figure 8.4: *A Dalitz plot showing the allowed region of the x_q-$x_{\bar{q}}$ plane for a $\gamma^\star \to q\bar{q}g$ event with massless partons.* The thick lines indicate the singularities where $x_q = 1$ and $x_{\bar{q}} = 1$. Their intersection marks the position of the soft gluon singularity: $x_g = 0$. The concept of jets will be introduced later, but it is clear that there has to be at least a certain angle between the gluon and the quarks if the jet in gluon direction is to be detected separately. Source: [27, p. 74].

So, how does one deal with these singularities to find a meaningful expression for the cross section to first order? Consider first the two-jet cross section. Two jets are detected when the gluon is either very soft or almost parallel to the quarks such that only two energy flows back-to-back can be measured. Including interference terms, the cross section in the case of an unresolved gluon is given by (integration over two-jet region, see Fig. 8.4)

where T stems from the criterion separating the two- and three-jet regions of the Dalitz plot: $\max\{x_q, x_{\bar{q}}, x_g\} < T$. The singularities of the second and third term cancel and the result is a function of the parameter T. However, our problem is not yet resolved, since $\lim_{T \to 1} f(T) = -\infty$.

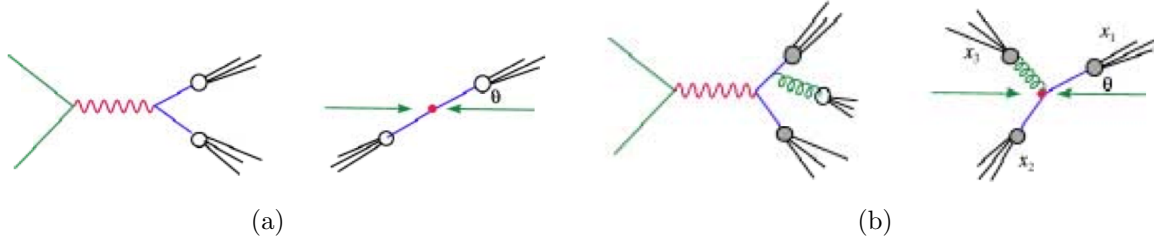If the gluon can be resolved, a three-jet event is detected and the integration is over the

Figure 8.5: *Hadronization of quarks and gluons.* Diagrams of the processes $e^+e^- \to q\bar{q} \to$ hadrons (a) and $e^+e^- \to q\bar{q}g \to$ hadrons (b). The RHS shows the situation in the center of mass frame. Source: [39, p. 5 and 6].

three-jet region of Fig. 8.4:

$$\sigma_{\text{three-jet}}(T) = \left| \text{} \right|^2 + \mathcal{O}(\alpha_s^2) = \sigma_0\alpha_s g(T) + \mathcal{O}(\alpha_s^2)$$

where $\lim_{T\to 1} g(T) = +\infty$. Combining the two-jet and three-jet cross sections, one finds that the dependence on T cancels yielding a finite result for the total cross section:

$$\sigma_{\text{tot}} = \sigma_{\text{two-jet}} + \sigma_{\text{three-jet}} + \cdots = \sigma_0 \left(1 + \alpha_s \left[f(T) + g(T)\right] + \mathcal{O}(\alpha_s^2)\right)$$

$$= \boxed{\sigma_0 \left(1 + \frac{3}{4}C_F \frac{\alpha_s}{\pi} + \mathcal{O}(\alpha_s^2)\right)}.$$

8.2 Jets and other observables

We now focus on entities actually observable in experiment. We do not observe free quarks but only colorless hadrons produced by the "hadronization/fragmentation" of quarks and gluons. For instance, the processes discussed so far can be visualized as in Fig. 8.5.

The anatomy of the process $e^+e^- \to Z \to$ hadrons is sketched in Fig. 8.6. The things that we can do based on such a process include

- Measure α_s,

- Measure the masses of (heavy) quarks,

- Measure gluon self-coupling,

- Study hadronization and particle correlations, and

- Study the transition between the non-perturbative and perturbative regime and the properties of quark or gluon jets.
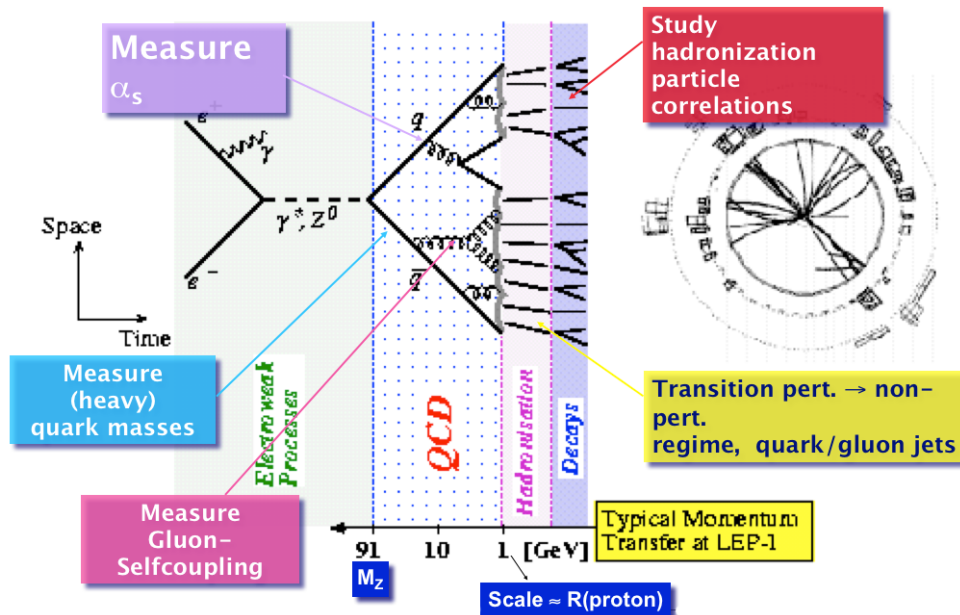
Figure 8.6: *The anatomy of the process $e^+e^- \rightarrow \gamma^\star, Z \rightarrow hadrons$.* Source: [40, p. 13, modified].

8.2.1   Jet algorithms

Let us turn to the question: What is a jet?

Fig. 8.7 shows a multi-jet event recorded by the ALEPH detector. A possible verbal definition of "jet" would be "cluster/spray of particles (tracks, calorimeter deposits) or flow of energy in a restricted angular region". Jets are the connection between the quarks and gluons of QCD and the signals actually measured in the detectors. If we are to extract this information from the data, we clearly need some kind of algorithmic definition of this concept: In the "final state" of many interesting interactions there are quarks and gluons. These are the fundamental particles of QCD. Confinement (see p. 148) means that in the detector we see hadrons (together with leptons and photons), but not single quarks or gluons. At energies much larger than $\Lambda^{\mathrm{QCD}}(\sim 1\,\mathrm{GeV})$ these hadrons appear confined into jets. Our aim is to compare the predictions based on partons (quarks and gluons) with the measurements on hadrons. Therefore, we need an algorithmic definition of a jet which

1. can be applied both to data *and* predictions and

2. gives a close relationship between partons and jets of hadrons.

The basic requirement for such an algorithm is applicability at all relevant levels of theory and experiment: partons, stable particles, measured objects (calorimeter objects, tracks, etc.) while always finding the same jet. Furthermore, the algorithm has to be independent of the very details of the detector, e.g. the granularity of the calorimeter, the energy
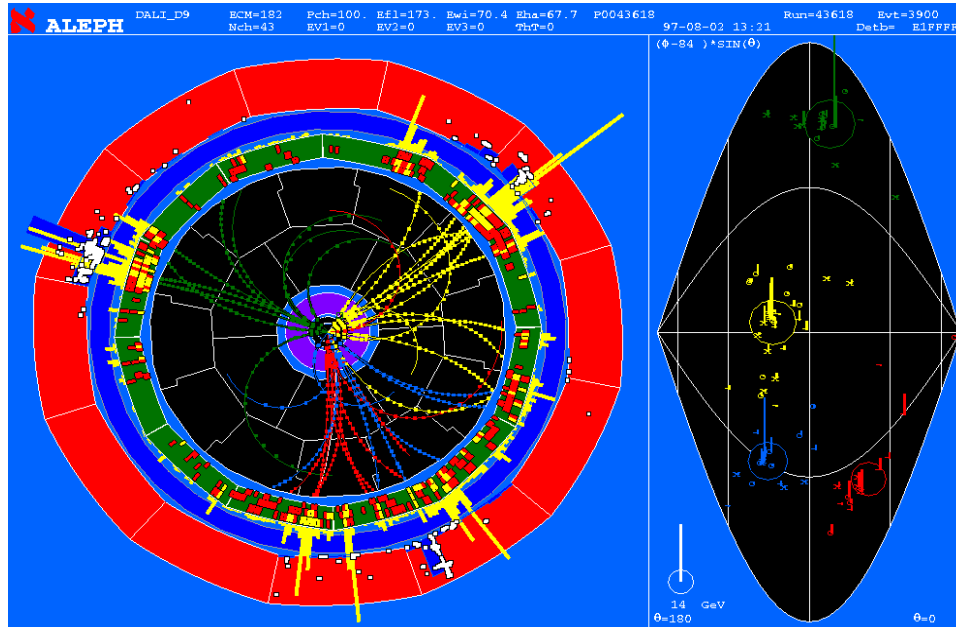
Figure 8.7: *Multi-jet event in the ALEPH detector.*

response, etc. Finally, it should also be easy to implement. In order that we can test QCD predictions, there has to be a close correspondence between the jet momentum (i. e. energy, momentum, and angle) at the parton level and at the hadron level.

NB: Other requirements might strongly depend on the specific application/measurement being performed: For a precision test of QCD there may be requirements which for an analysis of W decays or searches for new physics might not be necessary (e. g. infrared safety).

Further requirements come from QCD: We want to compare perturbative calculations with the data. Therefore, the algorithm has to be insensitive to "soft physics" which requires infrared safety and collinear safety.

Infrared safety requires that the configuration must not change when adding a further soft particle. This would be violated by the following behavior[2]:
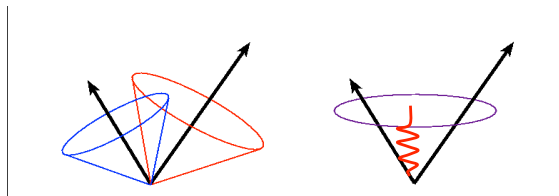
Collinear safety means that the configuration does not change when substituting one particle with two collinear particles. The problem is visualized in this figure:

---

[2]Source: [41, pp. 4].
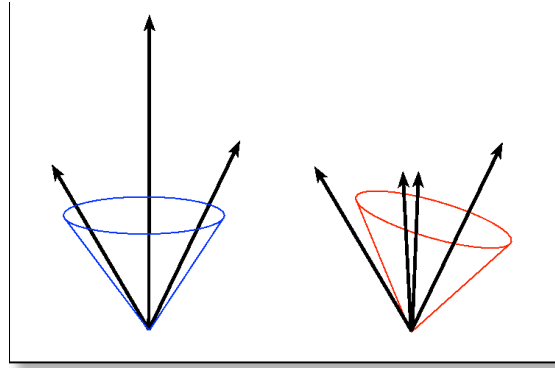
Infrared and collinear safety yield algorithms with the required insensitivity to soft physics: They guarantee the cancellation (between real and virtual emission diagrams) of the infrared and collinear divergencies in *every order* of perturbation theory.

8.2.1.1   Examples of jet algorithms

There are two classes of jet algorithms in use. Algorithms of the class "JADE" are used mainly for e^+e^- annihilations (i. e. for the analysis of events with purely leptonic initial states), but more recently, this class of jet algorithms is also used at hadron colliders. We will concentrate on this class here. The second class of jet algorithms is called "CONE" and is mainly used at hadron colliders with some applications also at e^+e^- colliders.

JADE class algorithms are characterized by

- a "metric" y_{ij} (measure of distance in momentum space),

- a criterion of resolution y_{cut}, and a

- procedure of recombination.

The original definition of the metric from the JADE experiment at PETRA reads

$$y_{ij} = \frac{2E_i E_j(1 - \cos\theta_{ij})}{E_{CM}^2} \approx \frac{m_{ij}^2}{E_{CM}^2} \tag{8.8}$$

where m_{ij} is the invariant mass of the particle pair (i, j), see Fig. 8.8(a) Given this metric and a pre-defined resolution y_{cut}, the algorithm is:
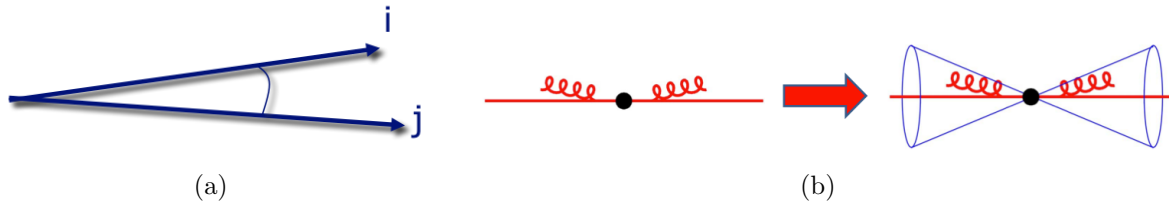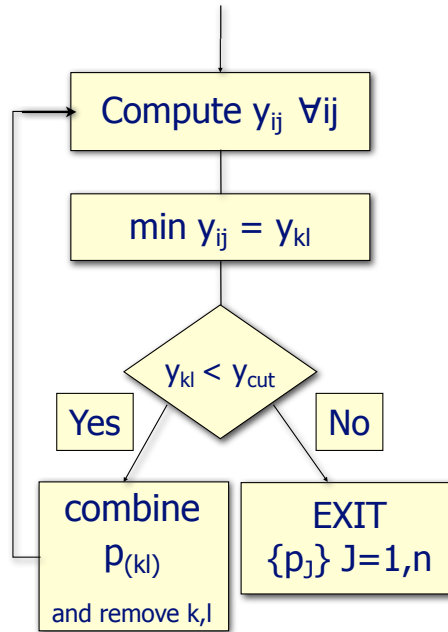
Figure 8.8: *Particle pair (a) and recombination of close particles (b).*

First, all distances y_{ij} between pairs (i, j) are calculated. Then we search for the smallest invariant mass: $\min_{(i,j)} y_{ij} = y_{kl}$. The fact that y_{kl} is the smallest distance in momentum space of all pairs (of particles or, in the subsequent steps, also pseudo-particles) means that the pair (k, l) is either nearly parallel, $\theta_{kl} = 0$, or one or both of the particles are very soft, see Fig. 8.8(b). If the distance cannot be resolved, $y_{kl} < y_{\text{cut}}$, the two particles (k, l) are combined (clustered) into one new pseudo-particle with the combined momentum $p_{(kl)} = p_k + p_l$ (i. e. momentum is conserved), see Fig. 8.9(a). This is the so-called E scheme. Applying this algorithm will reduce complex events until there is a certain number of jets left, as is sketched in Fig. 8.9(b).

The proposed algorithm has some very useful characteristics:

- Infrared safety,

$$y_{ij} \to 0 \text{ for } E_i \text{ or } E_j \to 0,$$

and collinear safety,

$$y_{ij} \to 0 \text{ for } \theta_{ij} \to 0,$$

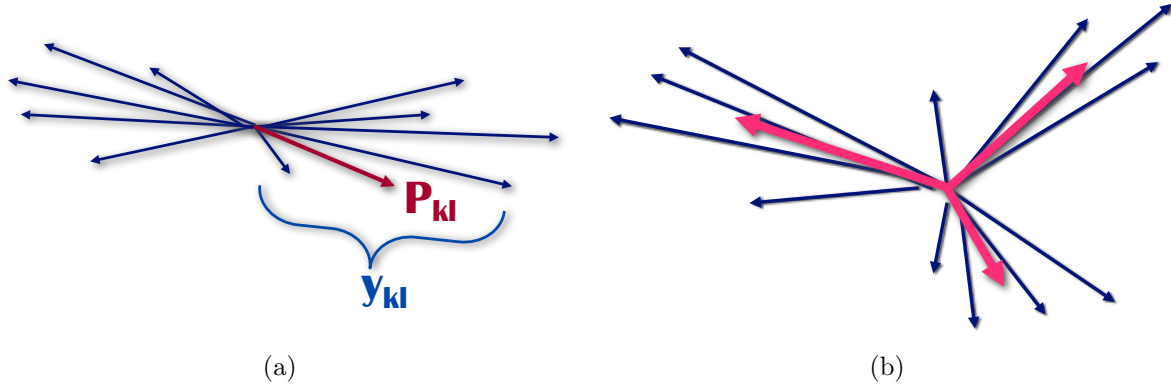(a)   (b)

Figure 8.9: *Recombination of particle pair with small invariant mass (a) and reduction of particle pattern to jets (b).*

(in every order of perturbation theory, see p. 161 and Eq. (8.8)).

- All particles are assigned to one and only one jet.

- The algorithm's sequence does not depend on y_{cut}.

- The number of found jets is a monotonic function of y_{cut}.

For the discussed algorithm there is no need to stick to the JADE metric of Eq (8.8); alternative metrics can be introduced. For instance, the DURHAM metric is

$$y_{ij} = \frac{2 \min\left(E_i^2, E_j^2\right)\left(1 - \cos\theta_{ij}\right)}{E_{CM}^2} \approx \frac{k_\perp^2}{E_{CM}^2} \tag{8.9}$$

where $k_\perp$ is the transverse momentum of the less energetic particle with respect to the more energetic one. The introduction of this metric was motivated by perturbative QCD calculations: It allows for the resummation of large logarithms of the type $\ln^m(y_{\text{cut}})$ in all orders of perturbation theory (see e. g. [27, pp. 139]). These logarithms appear order-by-order in the expressions for jet cross sections, jet rates, etc.

Now is a good time to recall the Dalitz plot of Fig. 8.4 where we separated a two-jet and a three-jet region. The algorithmic jet definition we have developed enables us to define the thee-jet region: Apply the jet algorithm until three jets are left. If the distance between the jets can be resolved, $\min_{(i,j)}(y_{ij}) > y_{\text{cut}}$, there are three jets, else it is a two-jet event. The shape of the found three-jet region is somewhat different, since y_{ij} also depends on the angle θ_{ij}, see Fig. 8.10.

In order to compare the analyzed data to the predictions of QCD, we need perturbative predictions for jet rates. For the reaction $e^+e^- \to$ hadrons the leading order predictions are as follows. For the JADE algorithm we have

$$\sigma_{\text{three-jet}}^{LO}(y_{\text{cut}}) = \sigma_0 C_F \frac{\alpha_s}{2\pi}\left[2\ln^2 y_{\text{cut}} + 3\ln y_{\text{cut}} - \frac{\pi^2}{3} + \frac{5}{2} - f(y_{\text{cut}})\right] \tag{8.10}$$
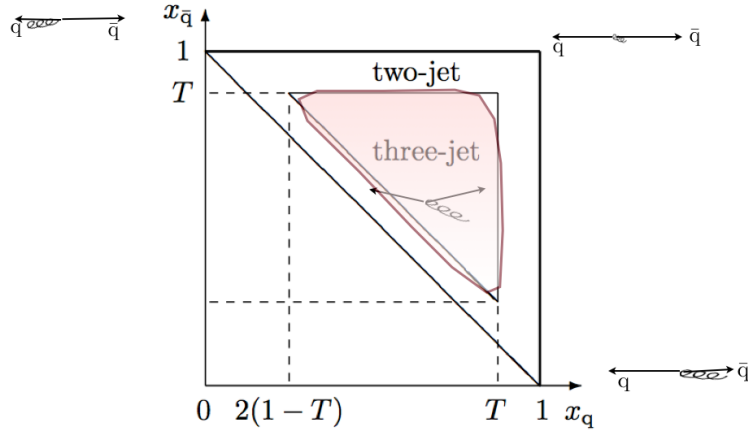
Figure 8.10: *A Dalitz plot showing the allowed region of the x_q-$x_{\bar{q}}$ plane for a $\gamma^\star \to q\bar{q}g$ event with massless partons.* The three-jet region is determined using an algorithmic jet definition.

where $f(y_{\text{cut}}) \to 0$ for $y_{\text{cut}} \to 0$. The prediction for the DURHAM algorithm is the same, except for the factor "2" in front of "$\ln^2 y_{\text{cut}}$". In simple terms, the logarithm terms arise because the vertex where the gluon is radiated off contributes a factor proportional to $\alpha_s/E_{\text{gluon}}$ to the integrand which upon integration yields $\int_{y_{\text{cut}}} dE/E$.

Resummation[3] with the DURHAM algorithm looks as follows. First, let

$$R_2(y_{\text{cut}}) = \frac{\sigma_{\text{two-jet}}}{\sigma_{\text{tot}}}.$$

One can show that

$$R_2 = \exp\left\{ -\int_{sy_{\text{cut}}}^{s} \frac{dq^2}{q^2} \frac{C_F \alpha_s(q^2)}{2\pi} \left[\ln\frac{s}{q^2} - \frac{3}{2} \right] \right\}$$

$$\approx 1 - \int_{sy_{\text{cut}}}^{s} \frac{dq^2}{q^2} \frac{C_F \alpha_s(q^2)}{2\pi} \ln\cdots + \cdots \approx 1 - \frac{C_F \alpha_s}{2\pi} \ln^2 y_{\text{cut}} + \ldots$$

where $R_2(y_{\text{cut}} \to 0) = 0$. This is an example of the characteristics an algorithm has to have if you want to perform "high-precision" perturbative QCD calculations. Now there also exists an algorithm of the k_t (DURHAM) type for hadron colliders, see later.

To conclude this section, we turn to the comparison of jet algorithms. There is no such thing as the best "benchmark" variable which allows to compare algorithms in a general manner. The suitability and performance of an algorithm depends very strongly on the performed analysis. Usually we would like to have a good resolution of energies and angles

---

[3]Resummation in QCD is analogous to the treatment of infrared divergencies in QED, see e.g. [14, pp. 202]
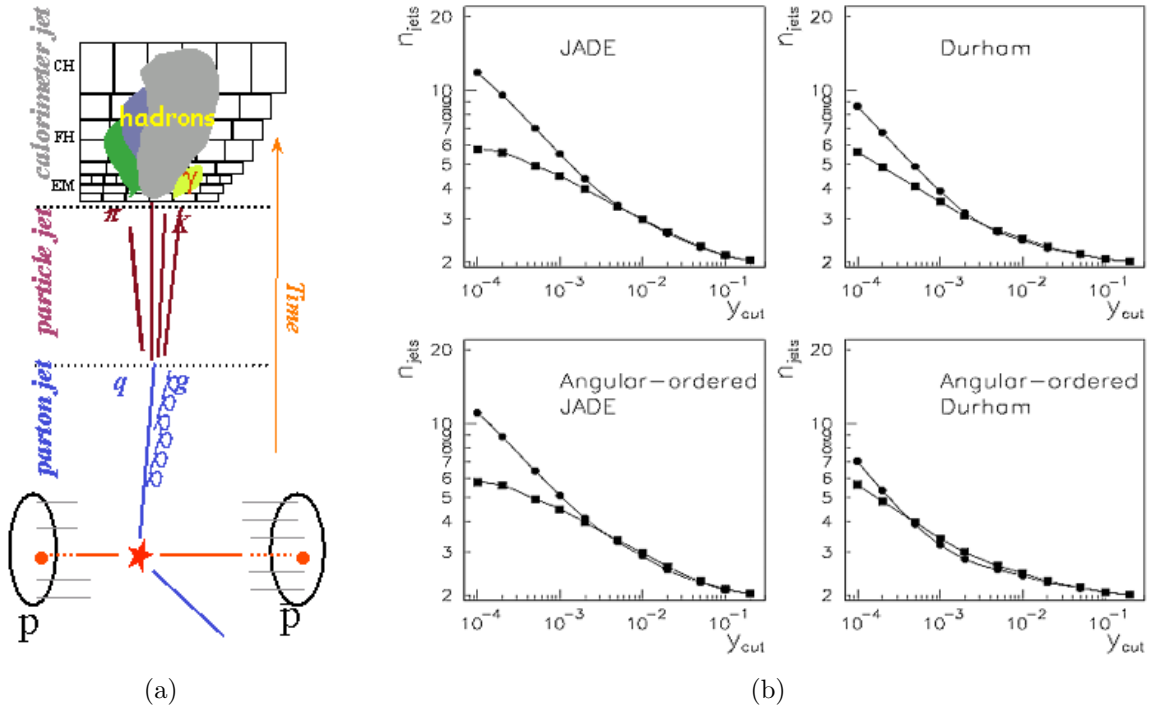
Figure 8.11: *Visualization of levels at which the algorithms have to deliver good resolution (a) and comparison of jet algorithms (b).* The mean number of jets is displayed as a function of y_{cut}. The parton level is denoted by squares and the hadron level by circles. The results were obtained by HERWIG Monte Carlo simulation at $E_{CM} = M_z$. Source: [34, p. 28]. For details compare [34, pp. 7].

of the jets at the parton, hadron, and detector levels (see Fig. 8.11(a) for a visualization), as well as a good efficiency and purity to find a certain number of jets at a certain level. For some jet algorithms, the mean number of jets as a function of y_{cut} at the hadron and parton levels, as obtained by HERWIG (Hadron Emission Reactions With Interfering Gluons) Monte Carlo simulation at $E_{CM} = M_Z$, is compared in Fig. 8.11(b). Another comparison[4] is shown in Fig. 8.12. The fraction of events with 2 jets which have 2, 3, 4, and 5 sub-jets is given as a function of y_{cut} or r^2, the radius fraction sqared, respectively. The data stem from HERWIG Monte Carlo simulations at $E_{CM} = 1.8\,\text{TeV}$ with $75\,\text{GeV} < E_t(\text{jet 2}) < 100\,\text{GeV}$. Data from a k_t algorithm are shown in Fig. 8.12(a) while the results in Fig. 8.12(b) come from a CONE algorithm with radius $R = 0.7$.

8.2.2   Event shape variables

The introduced jet algorithms can be used as a starting point to define more refined observables that capture the event topologies.

---

[4]More on k_t and CONE algorithms can be found in [41].
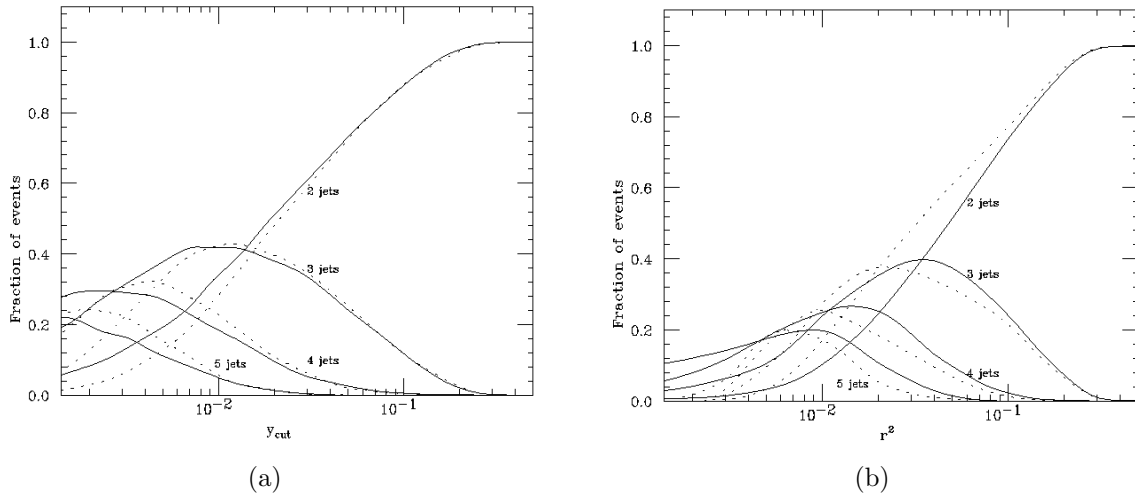
(a)   (b)

Figure 8.12: *Comparison of k_t (a) and CONE (b) algorithms.* Legend: —parton level, $\cdots$ calorimeter level. The fraction of two-jet events with 2, 3, 4, and 5 sub-jets is given as a function of y_{cut} or r^2. The data is generated by HERWIG Monte Carlo simulations at $E_{CM} = 1.8\,\text{TeV}$ with $75\,\text{GeV} < E_t(\text{jet 2}) < 100\,\text{GeV}$.

An example for an event shape variable is the *differential two-jet rate*. The definition goes as follows: Apply the DURHAM algorithm until exactly three jets are left (in contrast to the possibility to run the algorithm until a certain resolution is reached). Then take the minimal distance y_{ij} of all pairs (i, j) and call it y_{23} (or y_3): $\min_{(i,j)} y_{ij} = y_{23} = y_3$. This gives one value for each event. The distribution of these values for all events is an "event-shape distribution". Therefore, one can plot the differential cross section as in Fig. 8.13. There is one histogram entry for each event. The data come from hadronic Z decays at LEP. Observe that two-jet events are more likely than three-jet events. The perturbative regime is limited to high gluon energies. Hadronization effects that have to be phenomenologically modeled spoil the perturbative calculations at low y_3 values.

As another example for an event-shape variable, let us consider *thrust*. It was invented around 1978 and first used at PETRA. The idea is to select the axis that maximizes the sum of the longitudinal momentum components:

The thrust of an event is then defined as

$$T = \max_{\vec{n}} \frac{\sum_i |\vec{p}_i \cdot \vec{n}|}{\sum_i |\vec{p}_i|}$$

where $|\vec{n}| = 1$ and the sum runs over the three-momenta of all final states. The thrust axis is defined by the vector $\vec{n}_T$ for which the maximum is obtained. This definition means that for $T = 1$ the event is perfectly back-to-back while for $T = 1/2$ the event is spherically symmetric:
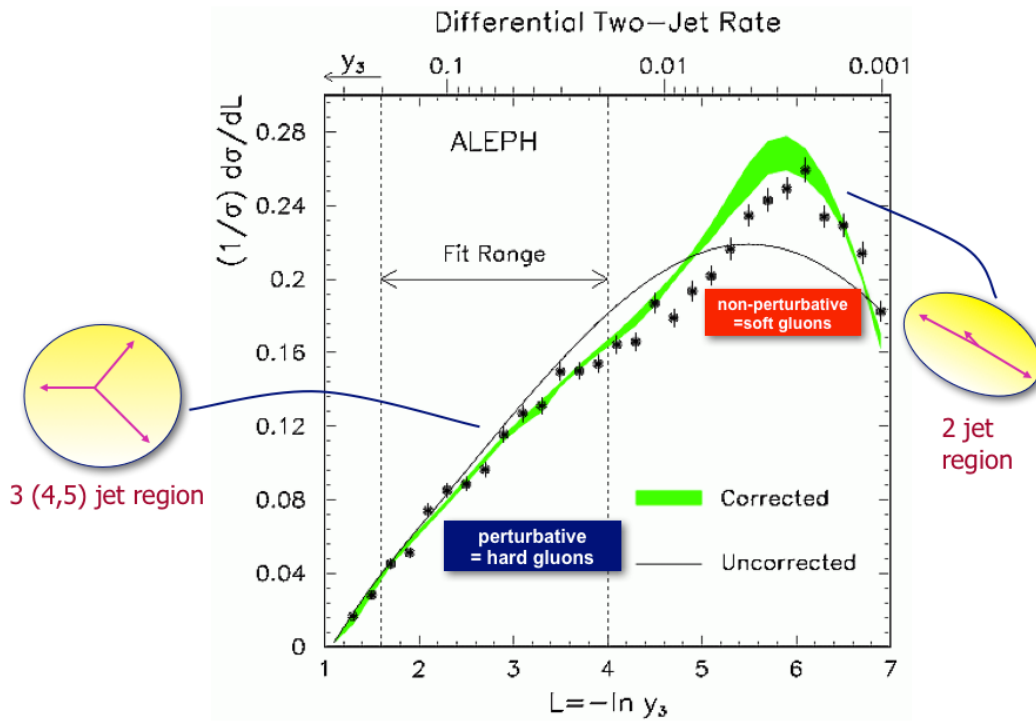
Figure 8.13: *Differential two-jet rate for hadronic Z decays at LEP.*

This point is also illustrated with ALEPH data of Z decays in Fig. 8.14 where Fig. 8.14(a) corresponds to $T \to 1$ and Fig. 8.14(b) to $T \to 1/2$. The corresponding event-shape distribution is shown in Fig.8.15 (compare also the differential two-jet rate event-shape distribution in Fig. 8.13).

There are further event-shape variables suitable for different purposes. Some examples are given in the following.

- *Thrust major T_{major}*: The thrust major vector $\vec{n}_{\mathrm{Ma}}$ is defined in the same way as the thrust vector $\vec{n}_T$, but with the additional condition that $\vec{n}_{Ma}$ must lie in the plane perpendicular to $\vec{n}_T$:

$$T_{\mathrm{major}} = \max_{\vec{n}_{\mathrm{Ma}} \perp \vec{n}_T} \frac{\sum_i |\vec{p}_i \cdot \vec{n}_{\mathrm{Ma}}|}{\sum_i |\vec{p}_i|}.$$

- *Thrust minor T_{minor}*: The minor axis is perpendicular to both the thrust axis and

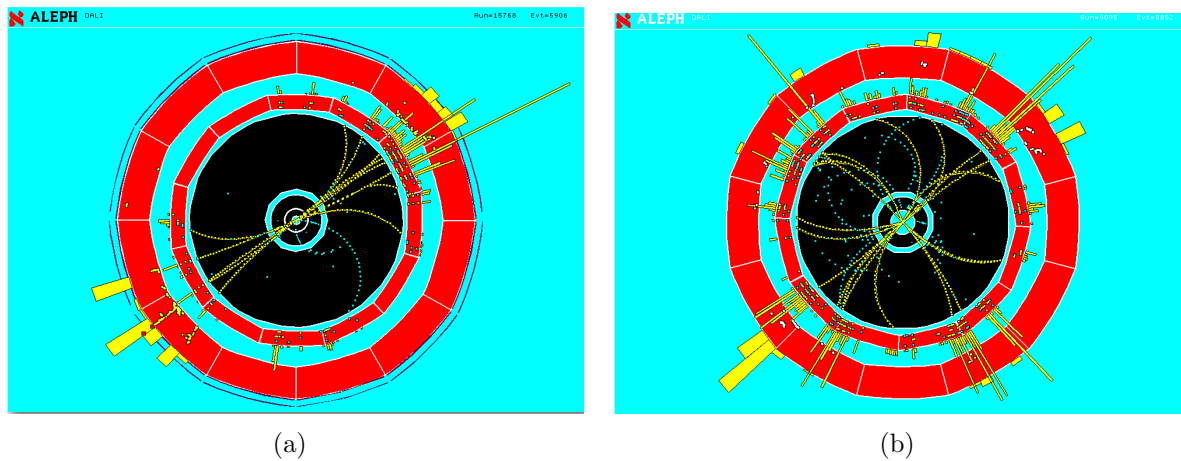(a)   (b)

Figure 8.14: *Event displays of Z decays recorded at ALEPH.* The thrust is nearly 1 for (a) and close to 1/2 for (b).
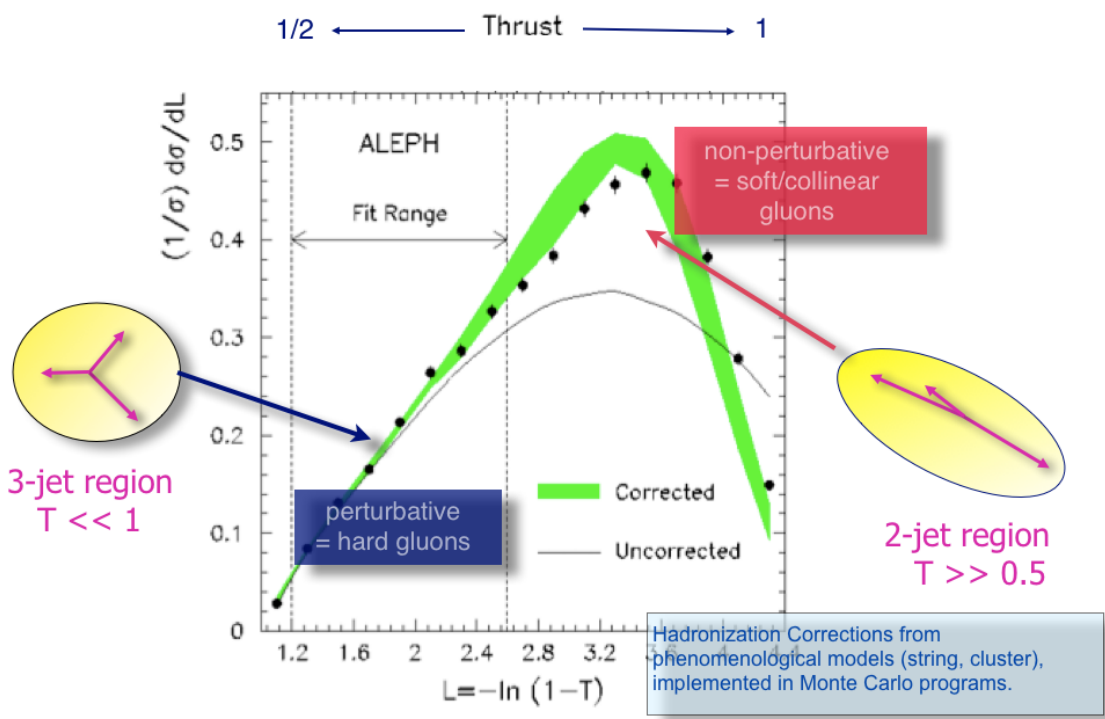

Figure 8.15: *Thrust for hadronic Z decays at LEP.* Observe that the two- and three-jet events are indicated by thrust values close to 1 and 1/2, respectively. Again, in the non-perturbative regime hadronization corrections from phenomenological models are needed.

the major axis: $\vec{n}_{\mathrm{Mi}} = \vec{n}_T \times \vec{n}_{Ma}$. The value of the thrust minor is given by

$$T_{\mathrm{minor}} = \frac{\sum_i |\vec{p}_i \cdot \vec{n}_{\mathrm{Mi}}|}{\sum_i |\vec{p}_i|}.$$

- *Oblateness O*: The oblateness is defined as the difference between thrust major and thrust minor:

$$O = T_{\mathrm{major}} - T_{\mathrm{minor}}.$$

- *Sphericity S*: The sphericity is calculated from the ordered eigenvalues $\lambda_{i=1,2,3}$ of the quadratic momentum tensor:

$$M^{\alpha\beta} = \frac{\sum_i p_i^\alpha p_i^\beta}{\sum_i |\vec{p}_i|^2}, \ \ \alpha, \beta = 1, 2, 3$$

$$\lambda_1 \geq \lambda_2 \geq \lambda_3, \ \ \lambda_1 + \lambda_2 + \lambda_3 = 1$$

$$S = \frac{3}{2}(\lambda_2 + \lambda_3).$$

The sphericity axis $\vec{n}_S$ is defined along the direction of the eigenvector associated to λ_1, the semi-major axis $\vec{n}_{\mathrm{sMa}}$ is along the eigenvector associated to λ_2.

- *Aplanarity A*: The aplanarity is calculated from the third eigenvalue of the quadratic momentum tensor:

$$A = \frac{3}{2}\lambda_3.$$

- *Planarity P*: The planarity is a linear combination of the second and third eigenvalue of the quadratic momentum tensor:

$$P = \lambda_2 - \lambda_3.$$

- *Heavy jet mass ρ*: A plane through the origin and perpendicular to $\vec{n}_T$ divides the event into two hemispheres, H_1 and H_2 from which the corresponding normalized hemisphere invariant masses are obtained:

$$M_i^2 = \frac{1}{E_{CM}^2} \left(\sum_{k \in H_i} p_k\right)^2, \ \ i = 1, 2.$$

The larger of the two hemisphere masses is called the heavy jet mass,

$$\rho = \max(M_1^2, M_2^2),$$

and the smaller is the light jet mass M_L,

$$M_L = \min(M_1^2, M_2^2).$$

- *Jet mass difference M_D*: The difference between ρ and M_L is called the jet mass difference:

$$M_D = \rho - M_L.$$

- *Wide jet broadening B_W*: A measure of the broadening of particles in transverse momentum with respect to the thrust axis can be calculated for each hemisphere H_i using the relation

$$B_i = \frac{\sum_{k \in H_i} |\vec{p}_k \times \vec{n}_T|}{2 \sum_j |\vec{p}_j|}, \quad i = 1, 2$$

where j runs over all particles in the event. The wide jet broadening is the larger of the two hemisphere broadenings,

$$B_W = \max(B_1, B_2),$$

and the smaller is called the narrow jet broadening B_N,

$$B_N = \min(B_1, B_2).$$

- *Total jet broadening B_T*: The total jet broadening is the sum of the wide and the narrow jet broadenings:

$$B_T = B_W + B_N.$$

- *C-parameter C*: The C-parameter is derived from the eigenvalues of the linearized momentum tensor $\Theta^{\alpha\beta}$:

$$\Theta^{\alpha\beta} = \frac{1}{\sum_i |\vec{p}_i|} \sum_i \frac{p_i^\alpha p_i^\beta}{|\vec{p}_i|}, \quad \alpha, \beta = 1, 2, 3.$$

The eigenvalues λ_j of this tensor define C by

$$C = 3(\lambda_1\lambda_2 + \lambda_2\lambda_3 + \lambda_3\lambda_1).$$

The discussed event-shape variables have been extensively used to analyze LEP data. Examples are given in Fig. 8.16: Fig. 8.16(a) shows thrust predictions and measurements; predictions and data for thrust, heavy jet mass, total jet broadening, wide jet broadening, and the C-parameter are shown in Fig. 8.16(b).
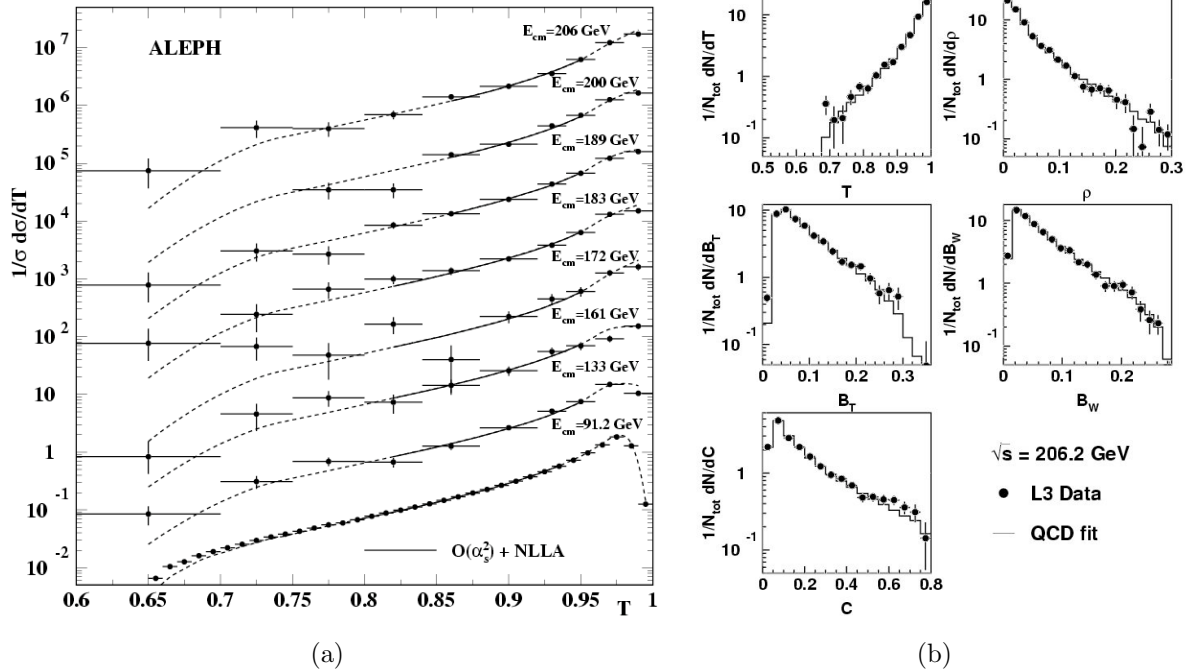
(a)   (b)

Figure 8.16: *Comparison of predictions and LEP data for some event-shape variables. Thrust data are shown for several center of mass energies (a). The other analyses deal with heavy jet mass, total jet broadening, wide jet broadening, and the C-parameter (b).*

8.2.3   Applications

Examples for applications of the observables discussed above in this section are measurements of the strong coupling constant α_s (see later, Sect. 8.3), the discovery of quark and gluon jets, measurements of the quark and gluon spin, the triple-gluon vertex, and jet rates or the analysis of differences between quark and gluon jets.

Quark jets were discovered at the SPEAR storage ring (SLAC) [42]. The data are shown in Fig. 8.17. For higher energies particles cluster around an axis and the Monte Carlo simulation based on a jet model fits the data better than the simulation based on an isotropic phase-space model. This is the first observation of a jet structure.

Gluon jets were discovered at PETRA (DESY) [43, 44, 45, 46]. Here, the relevant observable is oblateness (see p. 170). The first three-jet event seen by TASSO is shown in Fig. 8.18(a). In Fig. 8.18(b) one can observe that events at $E_{CM} \sim 30\,\text{GeV}$ exhibit larger oblateness (planar structure) than predicted by models without hard gluon radiation.

When it comes to parton spins the question is: How do you measure the spin of unobservable particles? For spin-1/2 fermions annihilating into a vector boson, conservation of angular momentum predicts a distribution
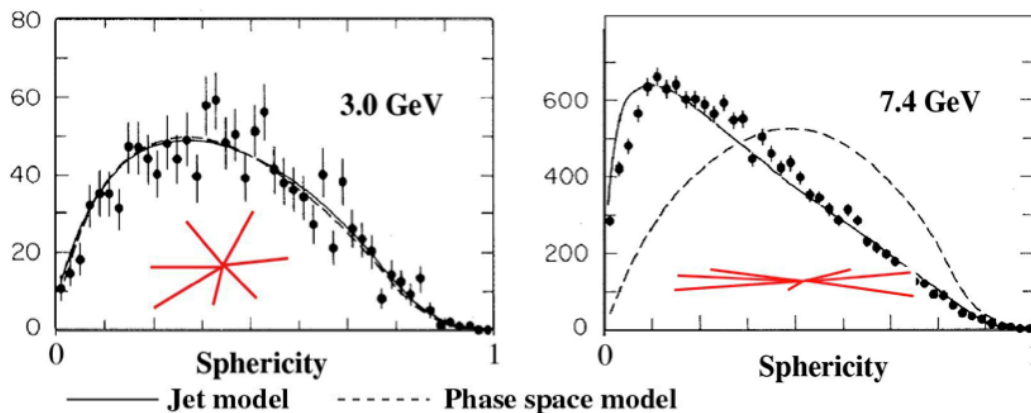
$$\frac{d\sigma}{d\cos\Theta^*} \sim 1 + \cos^2\Theta^*$$

Figure 8.17: *Discovery of quark jets at SPEAR (SLAC).* Observed sphericity (see p. 170) distributions for data, jet model (solid curves) and phase-space model (dashed curves) for $E_{CM} = 3\,\text{GeV}$ (LHS) and $7.4\,\text{GeV}$ (RHS). Source: [42, 38, p. 1611].
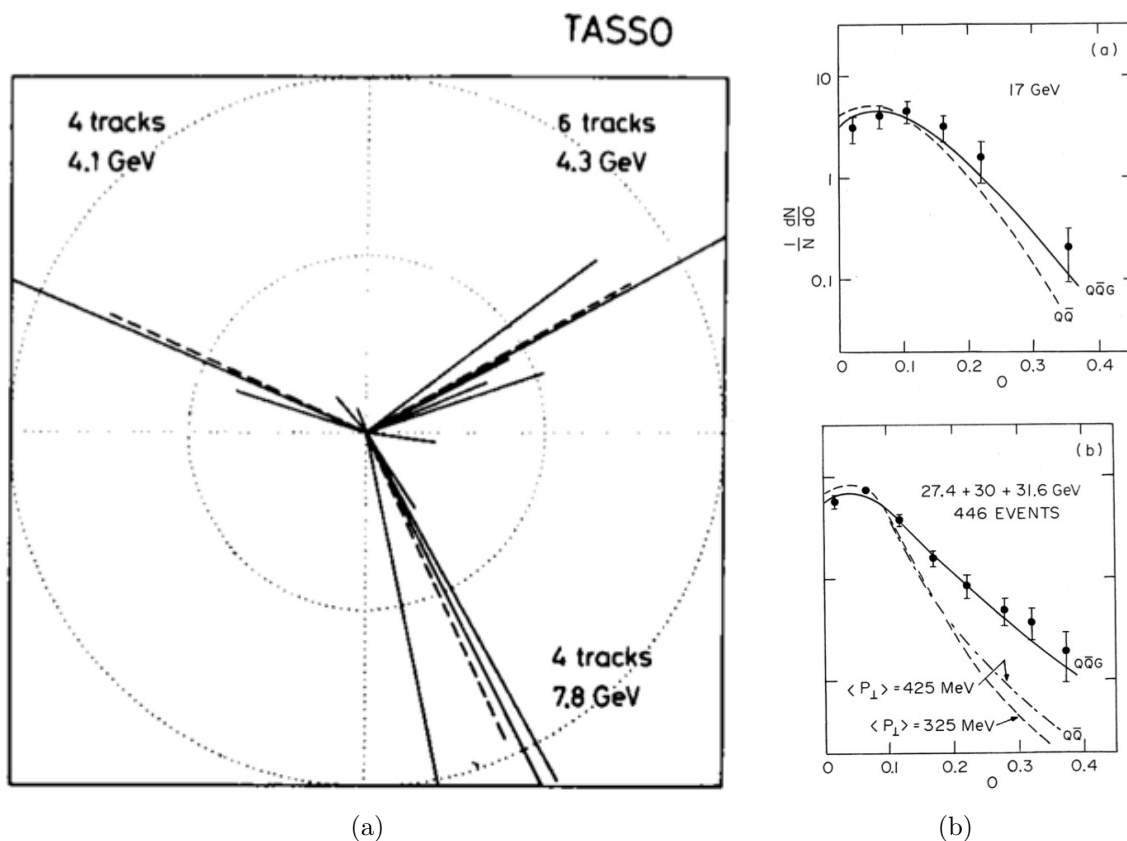

Figure 8.18: *The first three-jet event seen by TASSO (a) and the distribution $N^{-1}dN/dO$ as a function of oblateness, measured at MARK-J (b).* In both figures of (b) the solid curves are the predictions based on the $q\bar{q}g$ model and the dashed curve is based on the standard $q\bar{q}$ model. Source: [44, p. 832].
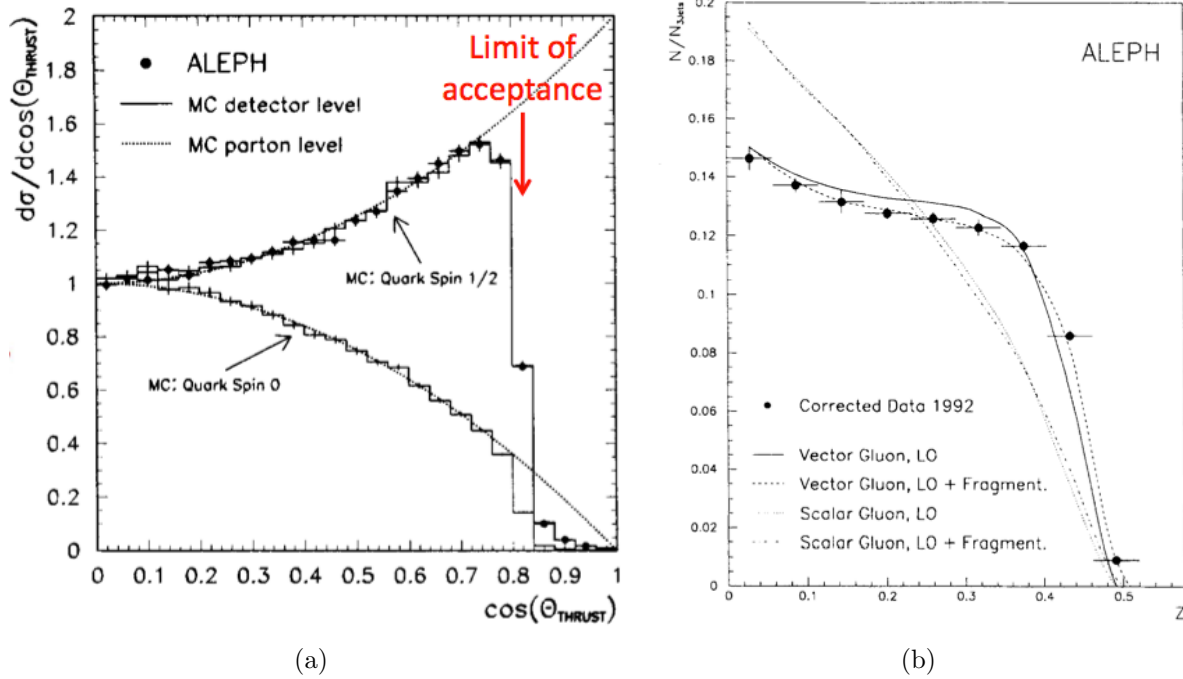
(a)   (b)

Figure 8.19: *Measurements of quark (a) and gluon (b) spin by ALEPH.* Source: [47].

if the final state particles have spin $1/2$ and

$$\frac{d\sigma}{d\cos\Theta^*} \sim 1 - \cos^2\Theta^* = \sin^2\Theta^*$$

for spin-0 particles in the final state. Therefore, the quark direction has to be measured to measure the quark spin. At LEP energies the thrust axis in two-jet events to a very good approximation aligns with the direction of the primary quarks. Thus, one can take the thrust direction in two-jet events. The exact expression for the spin-$1/2$ case reads

$$\frac{d\sigma}{d\cos\Theta^*} = \frac{\alpha_{\rm em}^2 e_q^2 \pi N_c}{2s} \left(2 - \beta_q^{*2} + \beta_q^{*2}\cos^2\Theta^*\right)\beta_q^*$$

where $\beta_q^* = \sqrt{1 - 4m_q^2/s} \to 1$ for $m_q = 0$. The resulting angular distribution found by ALEPH [47] is shown in Fig. 8.19(a).The experimental data are compared to a Monte Carlo simulation. The data are in perfect agreement with the spin-$1/2$ assignment for the quarks while a spin-0 assignment is clearly excluded. The sharp drop in the distribution around $\cos\Theta^* \sim 0.8$ is due to the finite detector acceptance.

Let us turn to the gluon spin. Hard gluon radiation leads to three-jet events. So, after applying a jet algorithm to select the three-jet events, how do we know which one is the gluon jet? Recall that the probability to radiate off a soft gluon is larger than to radiate off a hard gluon. Therefore, for three jets
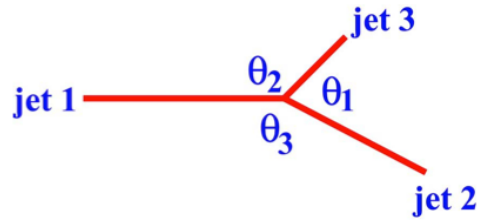
with energies

$$E_i = E_{CM}\frac{\sin\theta_i}{\sum_j \sin\theta_j},$$

if ordered by energy, $E_1 > E_2 > E_3$, jet 3 is the gluon jet in 75% of the events. Defining the variable

$$Z = \frac{1}{\sqrt{3}}(x_2 - x_3)$$

(recall $x_i = 2E_i/E_{CM}$), the Dalitz plot looks like in Fig. 8.20. The arrow length is proportional to the jet energy. The following cases have to be compared: In the spin-1 case ("vector gluon") the prediction reads

$$\frac{d^2\sigma^v}{dx_1 dx_2} \propto \left[\frac{x_1^2 + x_2^2}{(1-x_1)(1-x_2)} + \text{permutations}\,(1,2,3)\right]$$

while for spin-0 ("scalar gluon")

$$\frac{d^2\sigma^s}{dx_1 dx_2} \propto \left[\frac{x_3^2}{(1-x_1)(1-x_2)} + \text{permutations}\,(1,2,3) - 10\frac{\sum a_q^2}{\sum a_q^2 + v_q^2}\right]$$

where a_q and v_q are the axial-vector and vector couplings of the quarks to the intermediate photon or Z boson and the sums run over all contributing quark flavors. For e^+e^- annihilation via a photon only the vector coupling contributes, on the Z resonance both terms have to be taken into account. The ALEPH data shown in Fig. 8.19(b) clearly indicate that gluons have spin 1.

As we have seen before (see p. 145), the kinematic term of the QCD ($SU(3)$, non-abelian, gluon) Lagrangian contains a three-gluon term yielding a three-gluon vertex, a feature not present in QED ($U(1)$, abelian, photon). The splitting of a radiated gluon into two gluons will lead to a four-jet event, just like the splitting into a quark-antiquark pair:
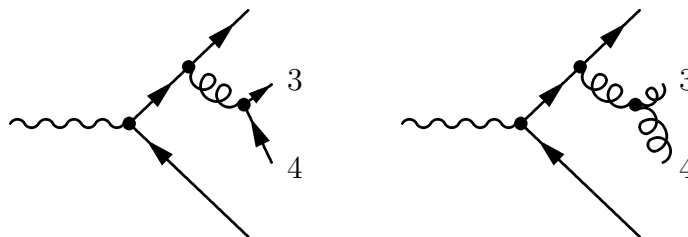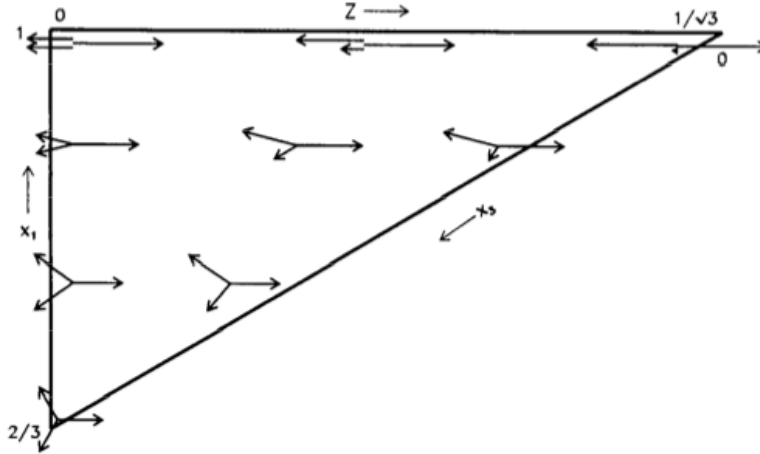
Figure 8.20: *Phase space as function of x_1 and Z for energy-ordered jet configurations,* $x_1 > x_2 > x_3$. The arrow length is proportional to the energy. Source: [47].

For gluon radiation off quarks one finds that the gluon is preferentially polarized in the plane of the splitting process. On the other hand, for a gluon splitting into two gluons there is a positive correlation between the plane spanned by the two new gluons and the polarization of the branching one. Finally, in case a gluon splits into two quarks, the plane defined by the momenta of the two quarks is anticorrelated with the polarization of the splitting gluon. So we conclude that for four-jet events induced by a gluon splitting into a $q\bar{q}$ pair, the distribution of the angle between the plane defined by the two primary quarks and the plane defined by the two secondary quarks should be enhanced around $90°$ (see Fig. 8.21). However, in a non-abelian theory we have contributions also from the triple-gluon interaction, and in this case the favored angle between the two planes spanned by the primary and secondary partons is rather small. Therefore, the shape of the distribution of this angle is sensitive to the color factors (see Sect. 7.4.1). Like in the three-jet case, it is difficult to distinguish between jets induced by the primary and the secondary partons. However, because of the $1/E$ characteristic of radiated gluons we expect the two secondary particles to be less energetic than the two primary quarks: If the jets are ordered by energy, $E_1 > E_2 > E_3 > E_4$, jets 3 and 4 are more likely to come from the radiated particles. So we arrive at the definition of the angular correlation variable called Bengtsson-Zerwas angle

$$\chi_{\mathrm{BZ}} = \angle\left[(\vec{p}_1 \times \vec{p}_2), (\vec{p}_3 \times \vec{p}_4)\right] = \frac{(\vec{p}_1 \times \vec{p}_2) \cdot (\vec{p}_3 \times \vec{p}_4)}{|(\vec{p}_1 \times \vec{p}_2)||(\vec{p}_3 \times \vec{p}_4)|}$$

where $\vec{p}_i$, $i = 1, \ldots, 4$ are the energy-ordered momenta of the four partons (jets). In Fig. 8.21 LEP measurements of χ_{BZ} are compared with the predictions by QCD on the one hand and an abelian model with three quark colors but no three-gluon coupling on the other. The data agree with QCD being an $SU(3)$ gauge theory rather than an abelian gauge theory.

At the end of our discussion of jet algorithms Fig. 8.12(a) is shown. It displays the fraction
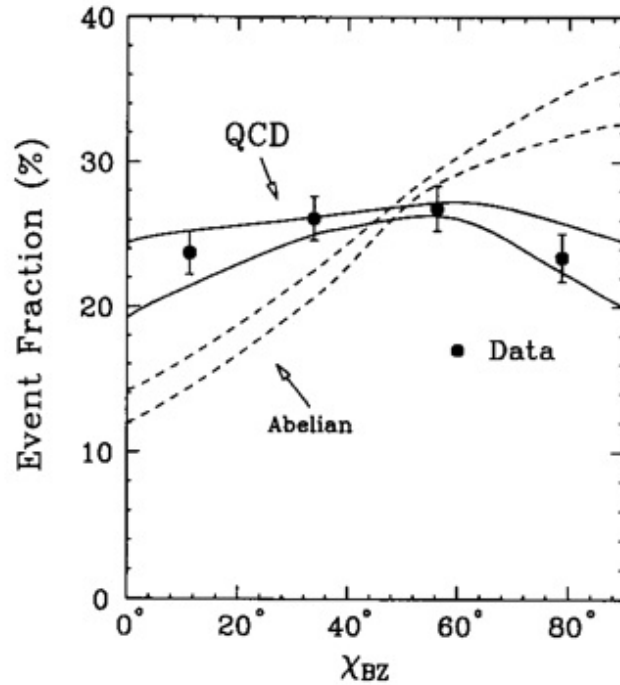
Figure 8.21: *Distribution of χ_{BZ} measured by L3.* The predictions for QCD and the abelian model are shown as bands indicating the theoretical uncertainties. Source: [48, p. 233].

of 2-jet events with 2, 3, 4, and 5 sub-jets as a function of y_{cut}. These predictions can be tested comparing measurements at highest LEP energies to Monte Carlo simulations which incorporate leading-order matrix elements for two-jet and three-jet production, plus approximations for multiple soft or collinear gluon radiation. Fig. 8.22 shows the n-jet rate according to the DURHAM (k_t) algorithm as a function of y_{cut}.

We conclude this section with a discussion of the differences between quark and gluon jets. Quark and gluon jets have different coupling strengths to emit gluons (see Sect. 7.4.1 and Fig. 8.23). Therefore, from couplings alone one expects a larger multiplicity in gluon jets of the order $C_A/C_F = 9/4$, and a softening of the momentum distributions for particles coming from the gluon jet. Thus gluon jets are more "soft" and "fat" than quark jets (see Fig. 8.24). Also the scaling violations, i. e. change of multiplicities with energy and momentum scale are different. In Fig. 8.24(d) the CONE algorithm is applied to data of OPAL (LEP) and compared to CDF data. The variable r denotes the radius of the considered cone fraction when R is the radius parameter of the cone algorithm:
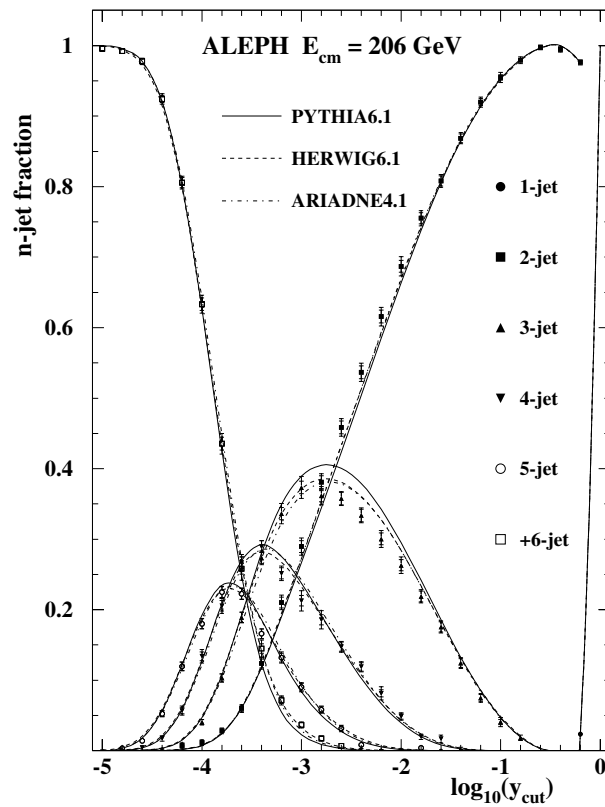
Figure 8.22: *ALEPH measurements of the n-jet rate (DURHAM) as a function of y_{cut}.*
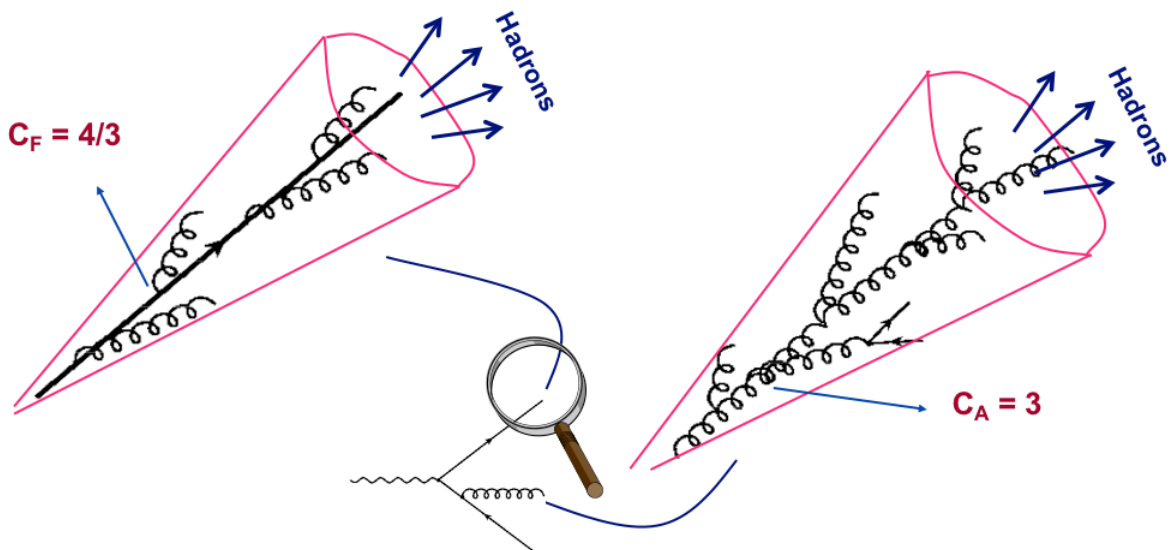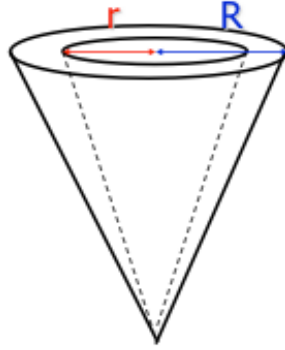

Figure 8.23: *Comparison of quark and gluon jets.* For a discussion of the difference in coupling strength see Sect. 7.4.1.

$\Psi(r)$ denotes the energy in a fraction of the cone and $\Phi(r)$ is defined by $\Phi(r) = d/dr\Psi(r)$.

8.3 Measurements of the strong coupling constant

The QCD Lagrangian is introduced in Sect. 7.4:

Except for the quark masses, there is only one free parameter in it: the strong coupling constant α_s which is discussed in Sect. 7.4.2. Recall that the differential equation for the strong coupling constant depending on the renormalization scale μ, $\alpha_s(\mu^2)$, is

$$\mu^2 \frac{\partial \alpha_s^2(\mu^2)}{\partial \mu^2} = \beta(\alpha_s(\mu^2))$$
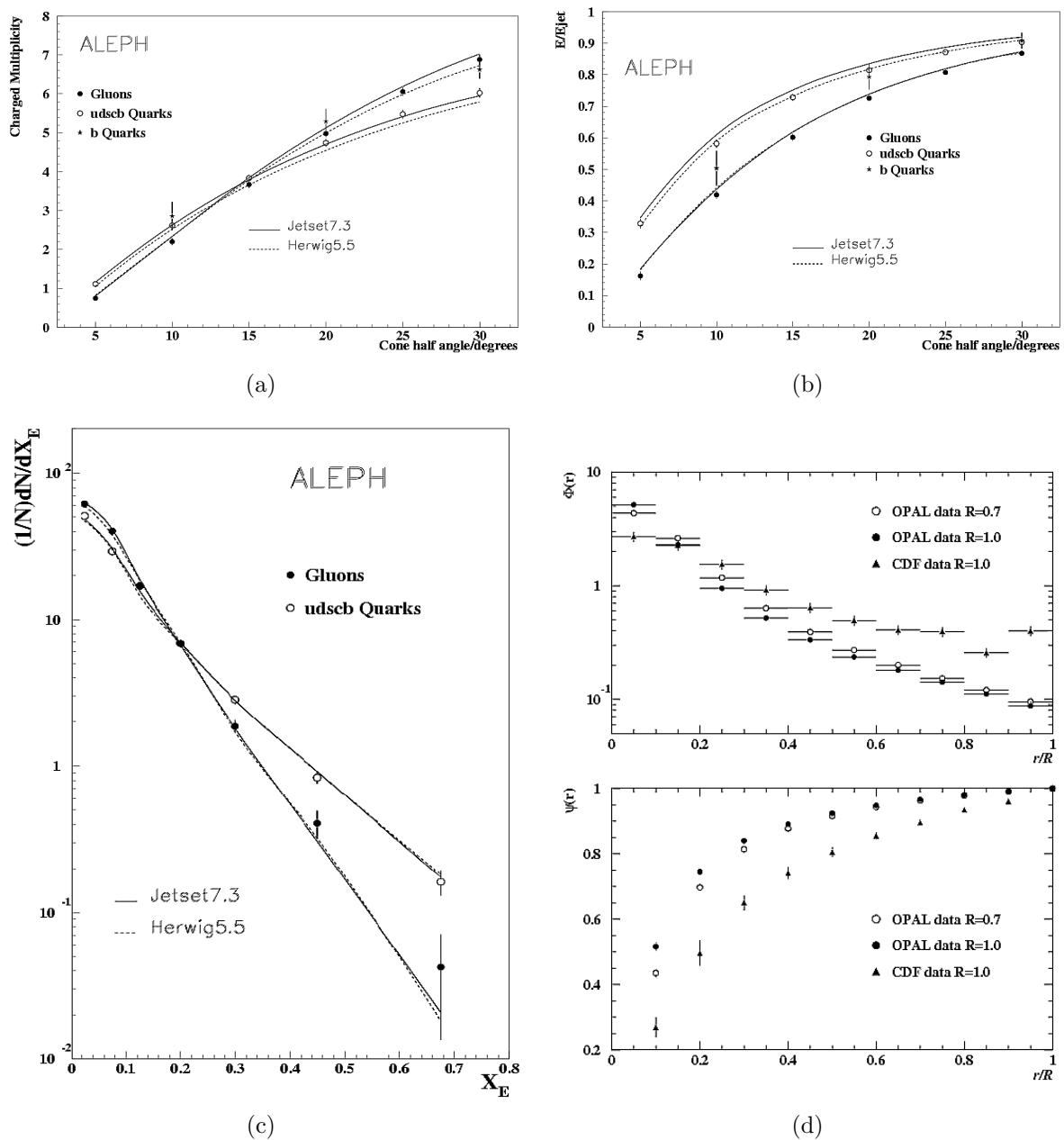
(a)

(b)

(c)

(d)

Figure 8.24: *Comparison of quark and gluon jets.* Note that gluon jets are more "soft" and "fat" than quark jets. The variable x_E is the energy fraction of the particles with respect to the jet energy (c). The variable r in (d) denotes the considered fraction of the cone.

which, retaining only the first term of the power expansion for β and absorbing the factor of 4π into the coefficient β_0, yields

$$\alpha_s(Q^2) \equiv \frac{g_s^2(Q^2)}{4\pi} = \frac{1}{\beta_0 \ln(Q^2/\Lambda_{\text{QCD}}^2)}.$$

At that point we also stressed that

$$\beta_0 = \frac{1}{4\pi}\left(11 - \frac{2}{3}n_f\right) > 0 \text{ for (the likely case of) } n_f < 17$$

which makes the effective coupling constant behave like shown in Fig. 7.4.2. The following expansion holds for $\alpha_s(\mu^2)$ (see Eq. (7.43)):

$$\alpha_s(\mu^2) \approx \alpha_s(Q^2)\left[1 - \alpha_s(Q^2)\beta_0 \ln\frac{\mu^2}{Q^2} + \alpha_s^2(Q^2)\beta_0^2 \ln^2\frac{\mu^2}{Q^2} + \mathcal{O}(\alpha_s^3)\right]. \qquad (8.11)$$

To measure the coupling strength one uses as many methods as possible in order to demonstrate that QCD really is the correct theory of strong interactions by showing that one universal coupling constant describes all strong interactions phenomena. Consider the perturbative expansion of the cross section for some QCD process:

$$\sigma^{\text{pert}} = \alpha_s(\mu^2)A + \alpha_s^2(\mu^2)\left[B + \beta_0 A \ln\frac{\mu^2}{Q^2}\right] + \mathcal{O}(\alpha_s^3) \qquad (8.12)$$

where the coefficients A and B depend on the specific process. So, if only the leading oder (LO) expansion is known, the following holds:
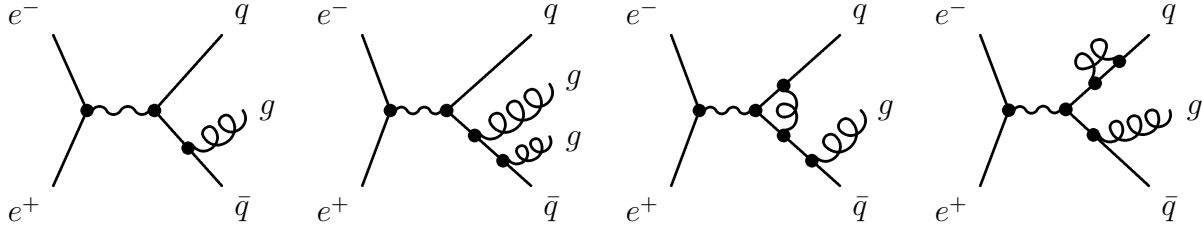
$$\sigma_{\text{LO}}^{\text{pert}} = \alpha_s(\mu^2)A = \alpha_s(Q^2)A - \alpha_s^2(Q^2)\beta_0 A \ln\frac{\mu^2}{Q^2} + \mathcal{O}(\alpha_s^2)$$

where in the second step we inserted the expansion from Eq. (8.11). This means that the result depends strongly on the choice of the renormalization scale μ. Since the corrections to the cross section can be relatively large, it is possible to find significantly different values for the measured effective coupling constant $\alpha_s^{\text{meas,eff}}$ for two different processes: Consider two processes, where the LO calculations predict

$$\sigma_{\text{LO};1}^{\text{pert}} = \alpha_s A_1$$
$$\sigma_{\text{LO};2}^{\text{pert}} = \alpha_s A_2.$$

The predictions are compared to the cross sections σ_1^{exp} and σ_2^{exp} from experiment. Finally, because of the said strong scale dependence, the result may be $\alpha_{s;1}^{\text{meas,eff}} \neq \alpha_{s;1}^{\text{meas,eff}}$.

To solve the problem of the correction depending on the renormalization scale being too large, one has to take the calculation to next-to-leading order (NLO) to reduce the scale dependence of the prediction. For our example reaction $e^+e^- \to q\bar{q}g$ this means

Figure 8.25: *Feynman diagrams for $e^+e^- \to q\bar{q}g$ to NLO.*

considering the diagrams shown in Fig. 8.25. The NLO expression is again obtained from the expansion in Eq. (8.12):

$$\sigma_{\text{NLO}}^{\text{pert}} = \alpha_s(\mu^2)A + \alpha_s^2(\mu^2)\left[B + \beta_0 A \ln \frac{\mu^2}{Q^2}\right] + \mathcal{O}(\alpha_s^3)$$

$$= \alpha_s(Q^2)A + \alpha_s^2(Q^2)B + \alpha_s^3(Q^2)\beta_0^2 A^2 \ln^2 \frac{\mu^2}{Q^2} + \mathcal{O}(\alpha_s^4)$$

where in the second line we inserted for $\alpha_s(\mu^2)$ the expansion from Eq. (8.11) and the dependence on $\ln(\mu^2/Q^2)$ cancels. Thus, the scale dependence of the prediction is much smaller than in the LO case. The scale dependence cancels completely at fully calculated order.

By comparing the NLO prediction for the cross section to experiment, one can extract $\alpha_s(Q^2)$, e. g. $\alpha_s(M_Z^2)$. This information can in turn be used to predict other process cross sections at NLO. Furthermore, by varying the scale μ^2 one can estimate the size of the NNLO contributions.

This procedure extends analogously to NNLO. Diagrams that have to be included at NNLO are shown in Fig. 8.26. The prediction reads

$$\sigma_{\text{NNLO}}^{\text{pert}} = \alpha_s(Q^2)A + \alpha_s^2(Q^2)B + \alpha_s^3(Q^2)C + \mathcal{O}\left(\alpha_s^4, \ln^3 \frac{\mu^2}{Q^2}\right)$$

where the scale dependence is reduced even further. NNLO is the lowest order at which scale variations at NLO can be tested.

As an example for the scale dependence of the extracted strong coupling constant, see Fig. 8.27 where $\alpha_s(M_Z^2)$ from jet rates at LEP is shown as a function of $\ln(\mu^2/Q^2)$. Note that the scale dependence is reduced by the extension to NLO, as mentioned before. The theoretical error is taken to be the range of values covered by the projection of the bands over $-1 < \ln(\mu^2/Q^2) < 1$ on the abscissa. The right figure shows how the central values and errors obtained this way for three different shape variables converge with improvements in the theory.

There has been an enormous progress in the measurements of the strong coupling during the last 20 years. This is due to major improvements on the theoretical and also the
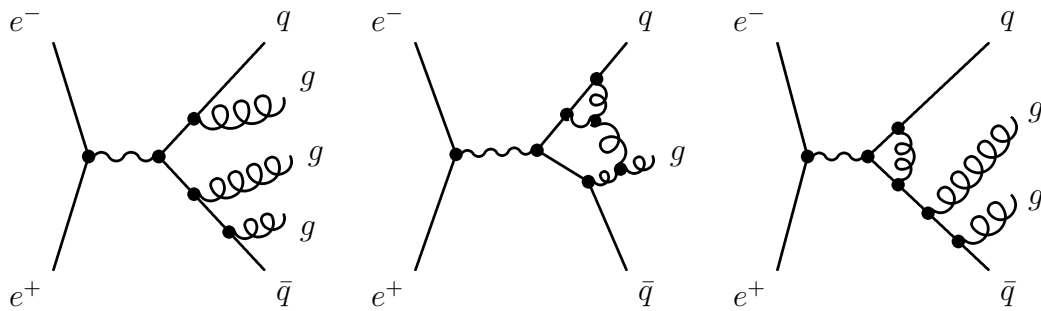
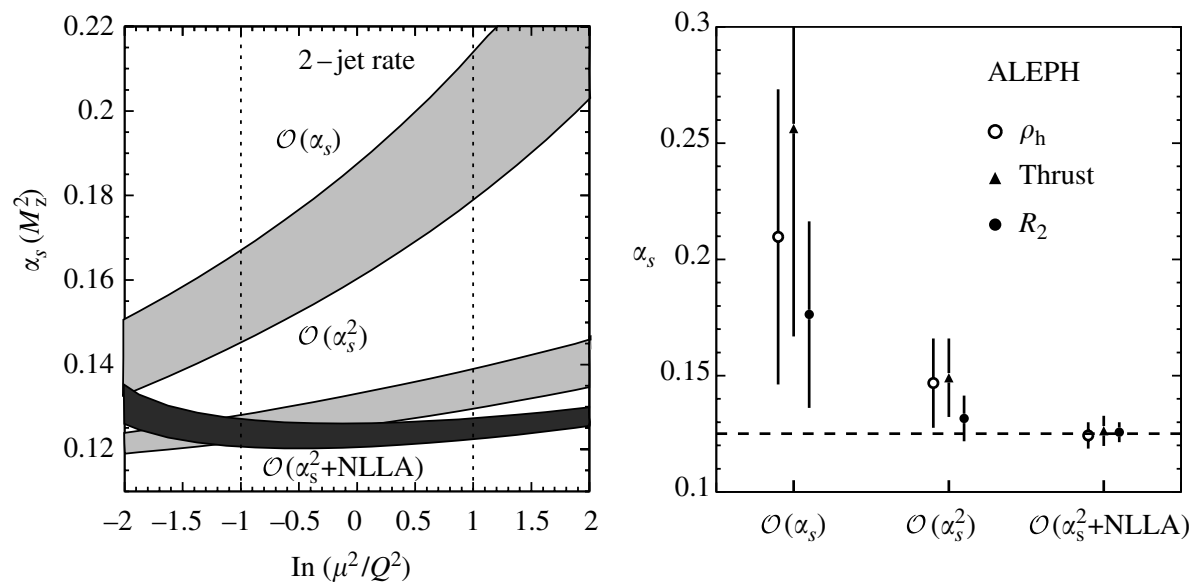Figure 8.26: *Feynman diagrams for $e^+e^- \to q\bar{q}g$ at NNLO.*

Figure 8.27: *Estimate of theoretical uncertainties for a measurement of the strong coupling constant from event shape variables.* NLLA refers to resummation of logarithms. Source: [27, p. 307].
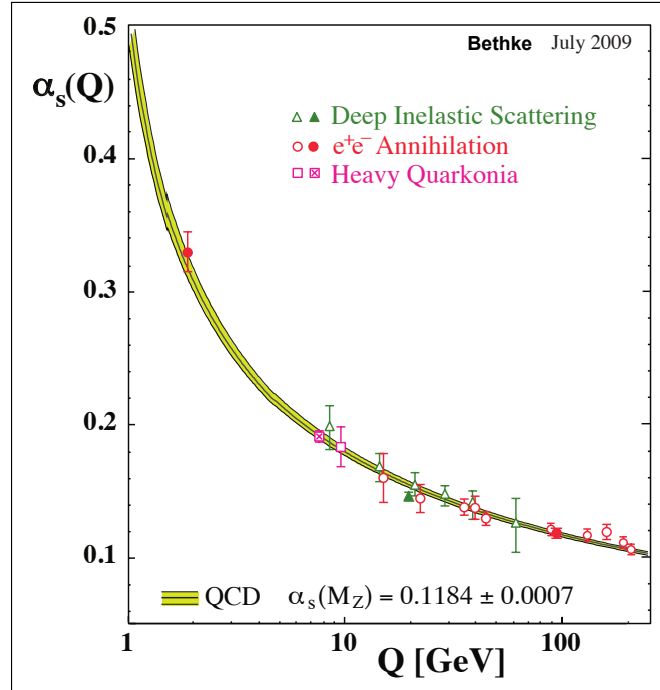
Figure 8.28: *Summary of measurements of α_s as a function of the respective energy scale Q. The curves are QCD predictions.* Source: [30, p. 12].

experimental side. A summary of measurements of α_s as a function of the respective energy scale Q is shown in Fig. 8.28.

In general, observables can be classified according to the influence the structure of the final state has on their value.

Inclusive observables do not look at the structure of the final state. Examples are total cross sections and ratios of cross sections (see e. g. Eq. (8.3)). Advantages of inclusive observables are that they do not (or only weakly) depend on non-perturbative corrections (hadronization) and that the perturbative series is now known to NNNLO. The disadvantage lies in the low sensitivity in some cases.

Non-inclusive (exclusive) observables, on the other hand, look at some structure in the final state depending on the momenta of the final state particles. Examples are jet rates and event shape distributions. Advantages of non-inclusive observables are high sensitivity and that the perturbative series is now known to NNLO (and resummation, see later). Disadvantages are that in some cases even the NNNLO corrections might be relevant and that hadronization (non-perturbative) corrections are needed.

As an example for the usage of inclusive observables, consider the determination of α_s from inclusive Z or τ decays. In general, the prediction of the cross section ratio R reads

$$R = \frac{\sigma^{Z,\tau \to \text{ hadrons}}}{\sigma^{Z,\tau \to \text{ leptons}}} = R_{\text{EW}}(1 + \delta_{\text{QCD}} + \delta_{\text{mass}} + \delta_{\text{np}})$$

where the overall factor R_{EW} depends on the electroweak couplings of the quarks.[5] The corrections are dominated by the perturbative QCD correction δ_{QCD}. The other terms take into account the finite quark masses and the non-perturbative corrections. The perturbative QCD correction term is given by

$$\delta_{QCD} = c_1 \frac{\alpha_s}{\pi} + c_2 \left(\frac{\alpha_s}{\pi}\right)^2 + c_3 \left(\frac{\alpha_s}{\pi}\right)^3 + \ldots.$$

Diagrammatically speaking, the factor R_{EW} arises from
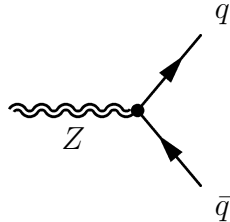
while the perturbative QCD corrections come from diagrams like in Fig. 8.25 and 8.26. For the case of

$$R_Z = \frac{\sigma^{Z \to \text{hadrons}}}{\sigma^{Z \to \text{leptons}}}$$

the prediction reads $R_{EW} = 19.934$, $c_1 = 1.045$, $c_2 = 0.94$, and $c_3 = -15$. The corresponding measurement is visualized in Fig. 8.29: Divide the number of hadronic decays by the number of leptonic decays to find $R_Z = 20.767 \pm 0.025$. From this ratio the following value of the strong coupling at the Z resonance can be extracted:

$$\alpha_s(M_Z) = 0.1226 \pm \underbrace{0.0038}_{\text{exp., mostly statistical}} \pm \underbrace{0.0002}_{M_t: \pm 5\,\text{GeV}} \pm \underbrace{0.0002}_{\text{renormalization shemes}}$$

$$= 0.1226 \begin{smallmatrix} +0.0058 \\ -0.0038 \end{smallmatrix}.$$

Finally, we state a new result from 2009, obtained using NNNLO predictions:

$$\alpha_s(M_Z) = 0.1193 \begin{smallmatrix} +0.0028 \\ -0.0027 \end{smallmatrix} \pm 0.0005.$$

We now turn to non-inclusive observables such as event-shapes and jet rates. We have already seen perturbative predictions for some examples of non-inclusive quantities in Sect. 8.2. There it is stated that the log terms in the predictions are because of the $\int dE/E$ integration arising from

$$\frac{d\sigma^{q \to qg}}{dE_{\text{gluon}}} \propto \sigma_0 \frac{\alpha_s}{2\pi} \frac{1}{E_{\text{gluon}}}$$

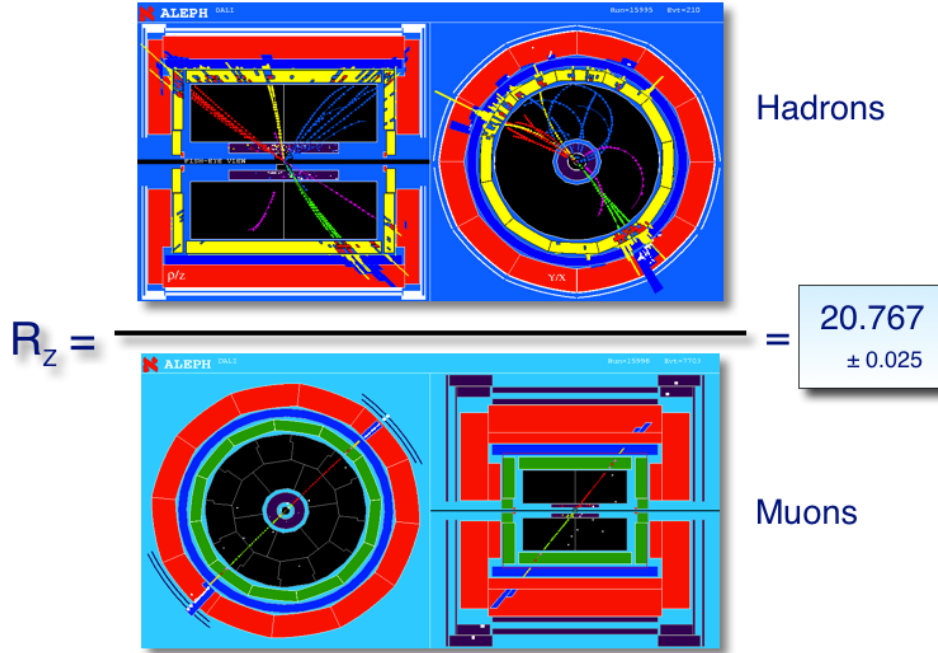[5] R_{EW} is a modified version of the ratio $R = N_c 11/9$ of Sect. 8.1.

Figure 8.29: *Visualization of R_Z measurement.*

where σ_0 is the Born cross section for $Z \to q\bar{q}$ (see Sect. 8.1). Recall that the perturbative prediction is given by:

$$\frac{1}{\sigma_0}\frac{d\sigma}{dx} = \alpha_s(\mu^2)A(x) + \alpha_s^2(\mu^2)\left[B(x) + \beta_0 A(x)\ln\frac{\mu^2}{Q^2}\right] + \mathcal{O}(\alpha_s^3)$$

where the coefficients A and B are calculable for the class of observables x which are infrared and collinear safe, i. e. infrared singularities from real and virtual radiative corrections cancel (thrust, jet rates, C-parameter, etc.). To recall the important example of thrust, see Fig. 8.15.

Let us take a look at the results obtained by NLO fits. First measurements gave indications that the missing higher order terms are large: The coupling constant should be the same for all variables, but the results vary too much (see Fig. 8.30) which indicates that the expansion to NLO does not suffice. Typical results obtained by NLO fits are

$$\alpha_s(M_Z) = 0.120 \pm 0.010.$$

As we have seen before, to obtain perturbative corrections, we have to do integrals of the type $\int_{y_{\text{cut}}}^{s} dE_{\text{gluon}}/E_{\text{gluon}}$ which gives rise to the logarithm terms in $\sigma_{\text{three-jet}}^{LO}$ (see Eq. (8.10)):

$$\sigma_{\text{three-jet}}^{LO} = \sigma_0 C_F \frac{\alpha_s}{2\pi}\left[\ln^2 y_{\text{cut}} + \dots\right]$$
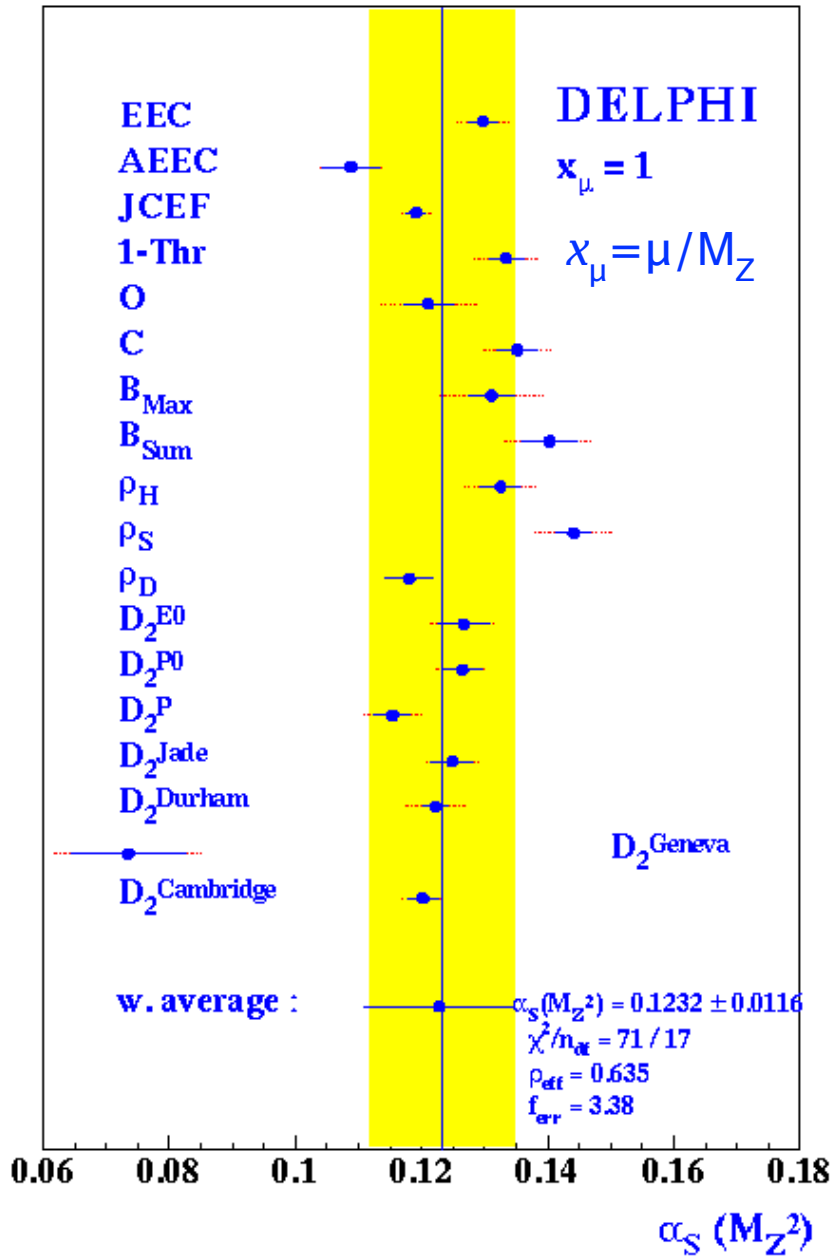
Figure 8.30: *NLO results for $\alpha_s(M_Z)$*. Source: [40, p. 29, modified].

where the color factor $C_F = 4/3$—the problem being that for $y_{cut} \to 0$ the series does not converge.[6] The resummation procedure mentioned earlier (see p. 165) also works for the three-jet rate:

$$R_3 = \frac{C_F \alpha_s}{2\pi} \ln^2 y_{cut} - \frac{C_F^2 \alpha_s^2}{8\pi^2} \ln^4 y_{cut} + \dots$$

$$= 1 - \exp\left\{-\int_{sy_{cut}}^{s} \frac{dq^2}{q^2} \frac{C_F \alpha_s(q^2)}{2\pi}\left[\ln\frac{s}{q^2} - \frac{3}{2}\right]\right\}.$$

Combined (to avoid double counting of logarithmic terms in resummed expressions and in full fixed order prediction) with full NLO calculations this gives theoretically much improved predictions. Typical results are:

$$\alpha_s(M_Z) = 0.120 \pm 0.005.$$

There are different sources of the remaining uncertainties. *Experimental uncertainties* include

- track reconstruction,

- event selection,

- detector corrections (via cut variations or different Monte Carlo generators),

- background subtraction (LEP2), and

- ISR corrections (LEP2).

They amount to about 1% uncertainty. Furthermore, there are *hadronization uncertainties* arising from the differences in behavior of various models for hadronization such as PYTHIA (string fragmentation), HERWIG (cluster fragmentation), or ARIADNE (dipole model and string fragmentation). Theses uncertainties are typically about 0.7 to 1.5%. Finally, there are also *theoretical uncertainties*, for instance

- renormalization scale variation,

- matching of NLO with resummed calculation, and

- quark mass effects.

---

[6]Recall that y_{cut} is the resolution parameter deciding if two particles are distinguished or seen as one pseudo-particle.
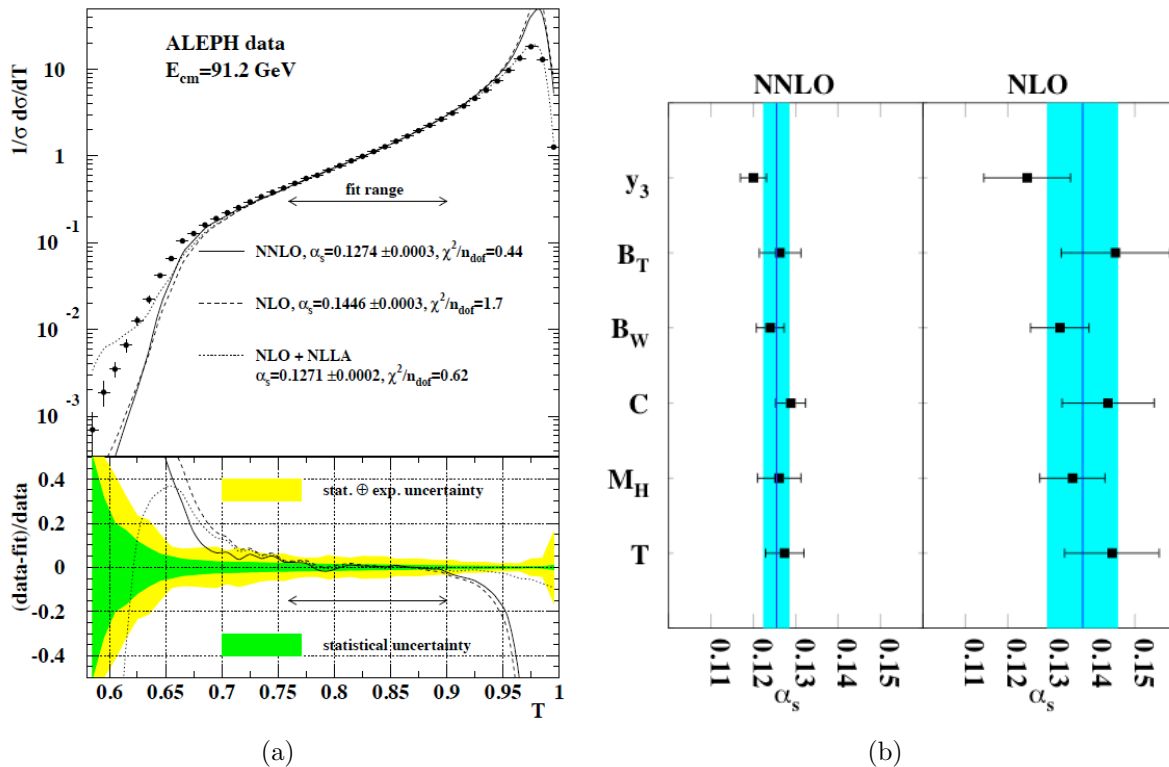
Figure 8.31: *NNLO fit to ALEPH thrust data (a) and visualization of improvement in NNLO over NLO (b).* Source: [50, p. 11 and 17].

The corresponding uncertainty is typically 3.5 to 5 %.

As we have seen, the perturbative predictions have to be to sufficiently high order if we are to accurately determine the strong coupling constant: Now a NNLO prediction is available. Bearing in mind the foregoing, it has to be of the form

$$\frac{1}{\sigma_0}\frac{d\sigma}{dy}(y, Q, \mu) = \alpha_s(\mu)A(y) + \alpha_s^2(\mu)B(y, x_\mu) + \alpha_s^3(\mu)C(y, x_\mu) + \mathcal{O}(\alpha_s^4)$$

where y denotes an event shape variable and $x_\mu = \mu/Q$. At this level of precision, one has to take care of additional issues, such as quark mass effects and electro-weak effects which typically contribute around or below the per-cent range.

The first determination of $\alpha_s(M_Z)$ based on NNLO (and NLLA) calculations of event shape distributions [49, 50] yields

$$\alpha_s(M_Z) = 0.1224 \pm 0.0009 \text{ (stat) } \pm 0.0009 \text{ (exp) } \pm 0.0012 \text{ (hadr) } \pm 0.0035 \text{ (theo)}.$$

The fit to ALEPH thrust data is shown in Fig. 8.31(a). The largely reduced scatter of values for different variables at NNLO is visualized in Fig. 8.31(b). Note that the reduced perturbative uncertainty is 0.003.

The most precise determination of the strong coupling constant is obtained from jet observables at LEP. Precision at the 2% level is achieved from the three-jet rate [51]:

$$\alpha_s(M_Z) = 0.1175 \pm 0.0020 \text{ (exp)} \pm 0.0015 \text{ (theo)}.$$

The three-jet rate is known to have small non-perturbative corrections and to be very stable under scale variations (for a certain range of the jet resolution parameter). For a comparison of LO, NLO, and NNLO predictions to the corresponding ALEPH data, see Fig. 8.32(a).

The LEP results concerning the determination of the strong coupling constant (see Fig.8.32(b)) can be summarized as follows (combination by S. Bethke, a couple of years ago).

- Tau decays (NNLO)

$$\alpha_s(M_Z) = 0.1181 \pm 0.0030$$

- R_Z (NNLO)

$$\alpha_s(M_Z) = 0.1226 \begin{array}{l} +0.0058 \\ -0.0038 \end{array}$$

- Event shapes (NLO + NNLO)

$$\alpha_s(M_Z) = 0.1202 \pm 0.0050$$

- All (not including recent NNNLO results)

$$\alpha_s(M_Z) = 0.1195 \pm 0.0035$$

- Latest world average (S. Bethke, 2009 [30])

$$\boxed{\alpha_s(M_Z) = 0.1184 \pm 0.0007}$$

8.4   Measurements of the QCD color factors

Because they determine the gauge structure of strong interactions, the color factors are the most important numbers in QCD, besides α_s. Discussing the triple-gluon vertex we concluded that our observables also allow to test the gauge structure of QCD. We have already learned that the color factors (for $SU(3)$) $C_F = 4/3$, $C_A = 3$, and $T_F = 1/2$ measure the relative probabilities of gluon radiation $(q \to qg)$, triple gluon vertex $(g \to gg)$, and gluon splitting $(g \to q\bar{q})$.
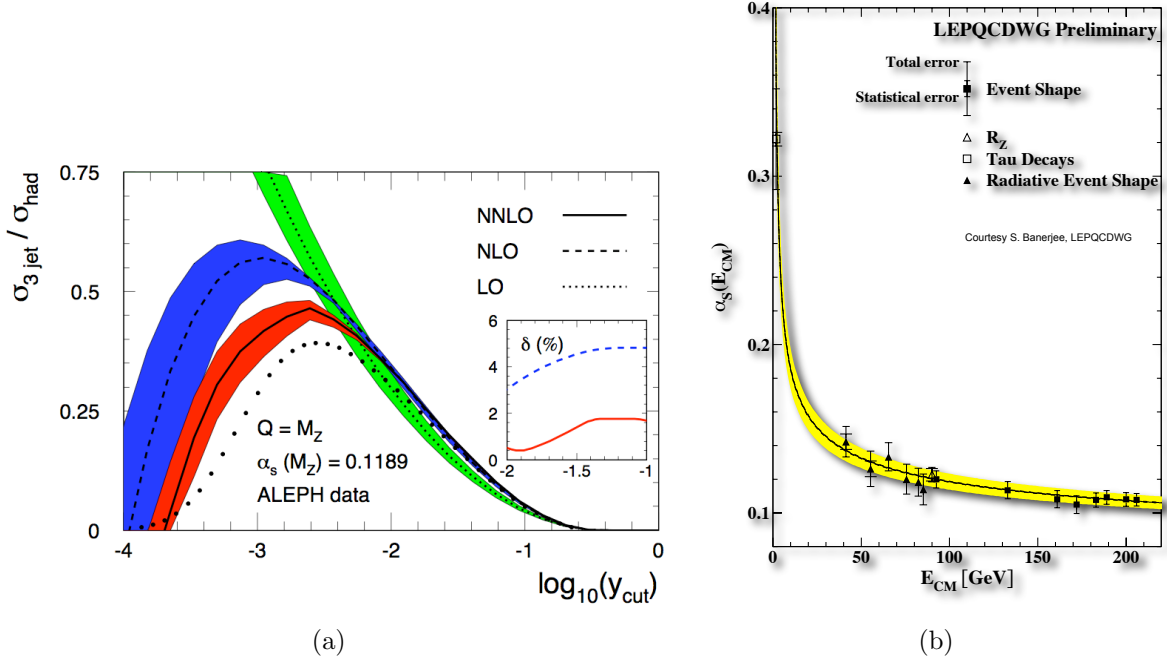
(a) (b)

Figure 8.32: *NNLO, NLO, and LO fits to ALEPH data for the thee-jet rate (a) and summary of LEP results for α_s (b).*

The cross section prediction for four-jet events at order α_s^2 can be shown to be

$$\frac{1}{\sigma_0}\frac{d\sigma_{\text{four-jet}}}{dy} = \frac{\alpha_s^2 C_F^2}{\pi^2}\left[\sigma_A(y) + \left(1 - \frac{1}{2}\frac{C_A}{C_F}\right)\sigma_B(y)\right.$$
$$\left. + \left(\frac{C_A}{C_F}\right)\sigma_C(y) + \left(\frac{T_F}{C_F}n_f\right)\sigma_D(y) + \left(1 - \frac{1}{2}\frac{C_A}{C_F}\right)\sigma_E(y)\right]$$

where σ_i, $i = A, \ldots, E$ are kinematic factors independent of the gauge group of QCD.

The combined measurements of the QCD color factors are summarized in Fig. 8.33: Four-jet and event shape results have been combined accounting for correlations between the measurements. In addition, constraints on C_A/C_F from differences between quark and gluon jets (see p. 177) are included. This yields

$$C_A = 2.89 \pm 0.21$$
$$C_F = 1.30 \pm 0.09$$

which is precise to 7% and agrees with the $SU(3)$ values of $C_A = 3$ and $C_F = 1.33$.

8.5 Hadronization

The trouble with hadronization is that perturbative calculations are no longer useful since α_s ceases to be comparatively small at length scales of about the proton radius.
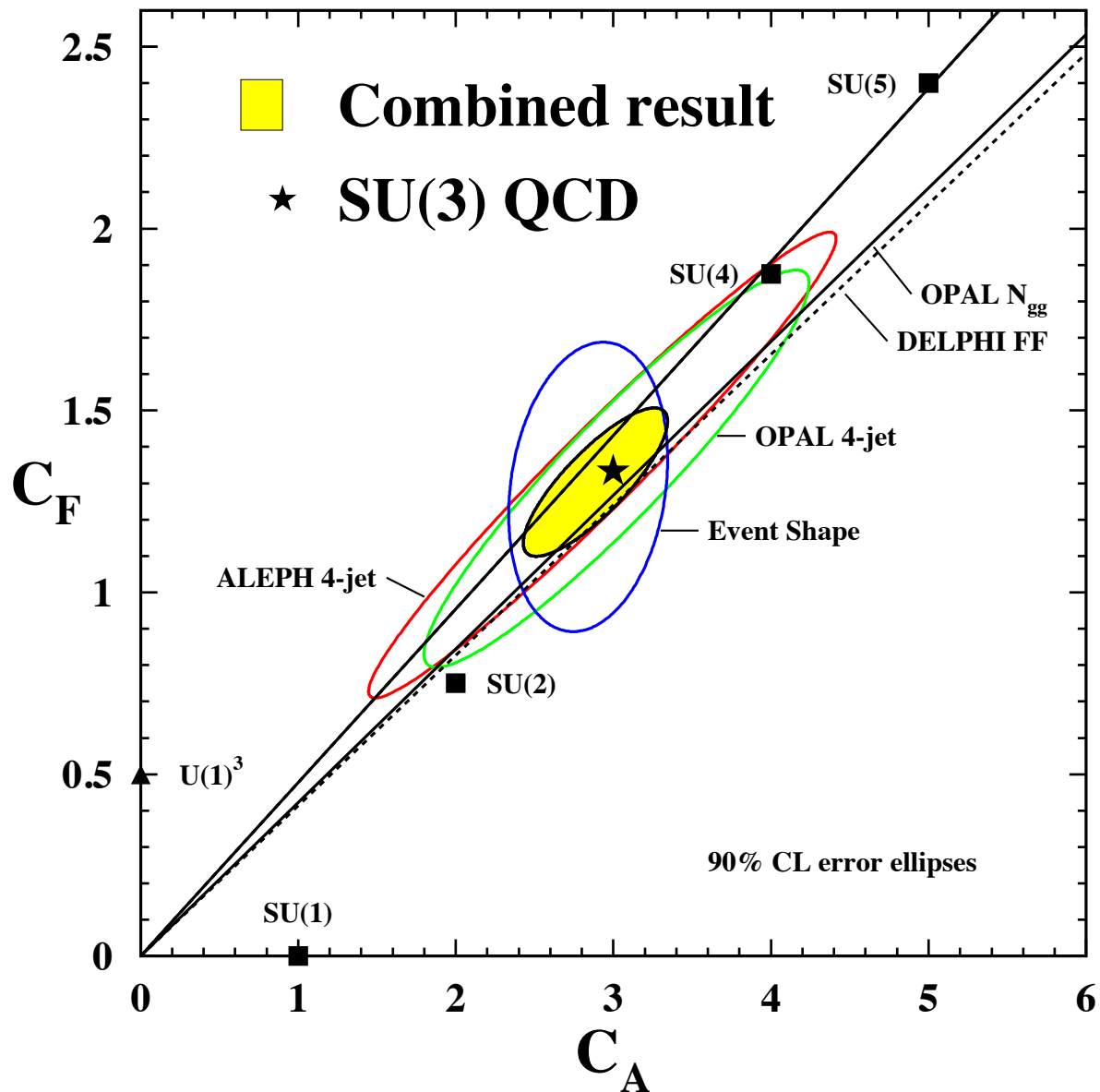
Figure 8.33: *Combined measurements of the color factors C_A and C_F. The ellipses show the correlated measurements using four-jet events or event shape distributions while the lines represent the results of determinations of C_A/C_F from DELPHI (dashed) and OPAL (solid). Source:* [52, p. 82].
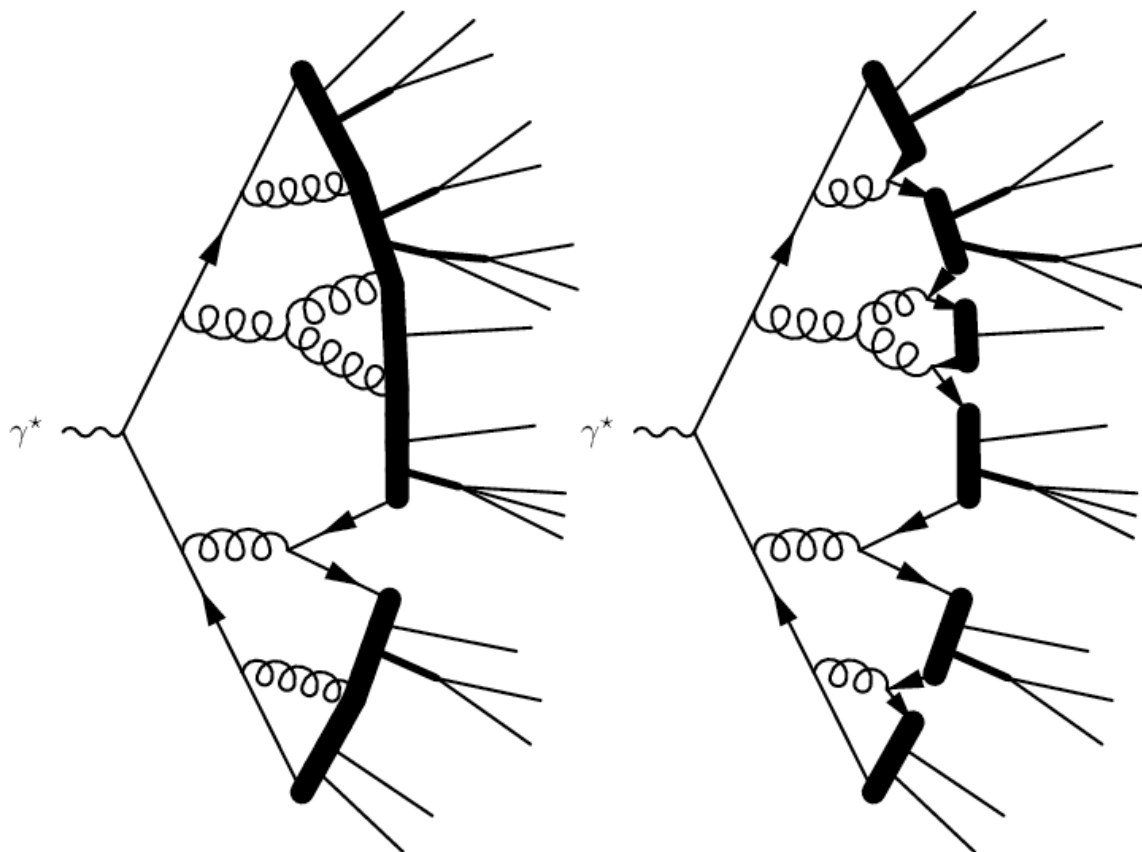
Figure 8.34: *Visualization of phenomenological models of hadronization.* (LHS) string fragmentation: JETSET/PYTHIA; (RHS) Cluster fragmentation: HERWIG. Source: [27, p. 164]

Perturbative QCD is applicable to the transition from the primary partons to a set of final state partons. This is pictured as a cascading process that is dominated by the collinear and soft emissions of gluons and mainly light quark-antiquark pairs. By contrast, phenomenological models are used to describe the non-perturbative transition from these final state partons to hadrons which then may decay according to further models (recall Fig. 8.6).

The parameters determining the behavior of the numerical models have to be adjusted using experimental data. Hadronization can be modeled by string fragmentation (JETSET/PYTHIA) or cluster fragmentation (HERWIG). For a visualization of this difference, see Fig. 8.34.

Fig. 8.35 shows comparisons of simulations to ALEPH data for hadron momentum distributions of the final state: Fig. 8.35(a) shows simulation and data for an inclusive variable and Fig. 8.35(b) deals with pions, kaons, and protons, respectively.
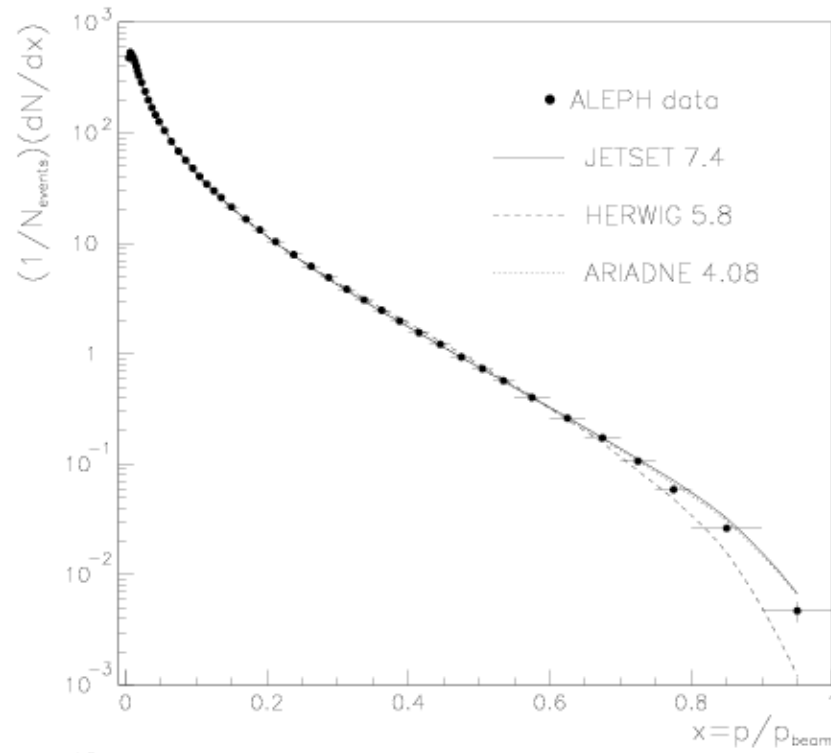
(a)
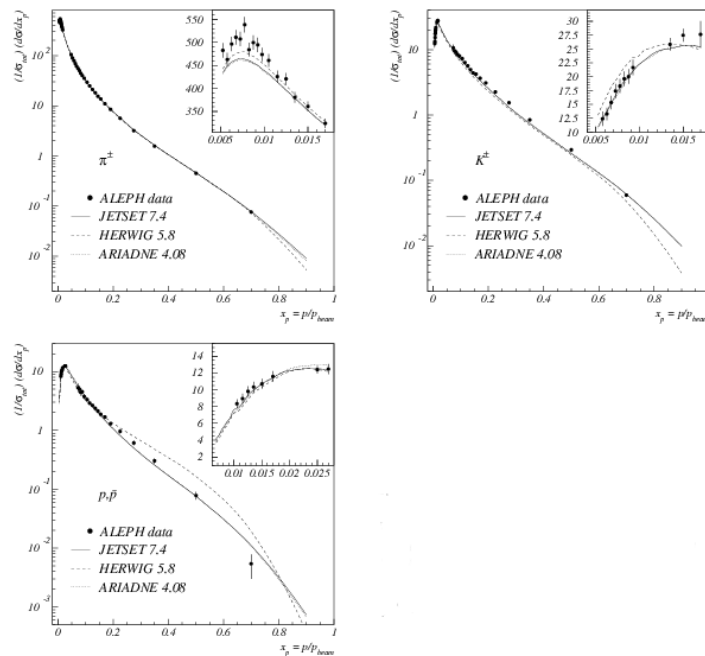
(b)

Figure 8.35: *Hadron momentum distributions, ALEPH data and simulation.* Inclusive measurement (a) and differential cross section for pions, kaons, and protons (b) compared with the predictions of JETSET, HERWIG, and ARIADNE. All observables are shown as functions of $x = p_{\text{hadron}}/p_{\text{beam}}$.